

Dynamic Optimization of Proton Exchange Membrane Water Electrolyzers Considering Usage-Based Degradation

Landon Schofield¹, Benjamin Paren², Ruaridh Macdonald³, Yang Shao-Horn⁴, and Dharik Mallapragada⁵

¹Department of Chemical Engineering, Massachusetts Institute of Technology

²Department of Chemical Engineering and Materials Science, Stevens Institute of Technology

³MIT Energy Initiative

⁴Department of Mechanical Engineering, Massachusetts Institute of Technology

⁵Department of Chemical and Biomolecular Engineering, New York University

Abstract

We present a techno-economic optimization model for evaluating the design and operation of proton exchange membrane (PEM) electrolyzers, crucial for hydrogen production powered by variable renewable electricity. This model integrates a 0-D physics representation of the electrolyzer stack, complete mass and energy balances, operational constraints, and empirical data on use-dependent degradation. Utilizing a decomposition approach, the model predicts optimal electrolyzer size, operation, and necessary hydrogen storage to satisfy baseload demands across various technology and electricity price scenarios. Analysis for 2022 shows that including degradation effects raises the levelized cost of hydrogen from \$4.56/kg to \$6.60/kg and decreases stack life to two years. However, projections for 2030 anticipate a significant reduction in costs to approximately \$2.50/kg due to lower capital expenses, leading to larger stacks, extended lifetimes, and less hydrogen storage. This approach is adaptable to other electrochemical systems relevant for decarbonization.

1 Introduction

Policies emphasizing economy-wide decarbonization are increasingly focused on promoting production of low-carbon hydrogen (H_2) to address emissions from difficult-to-electrify end-uses. For example, the emissions-indexed production tax credit (PTC) for H_2 as part of the Inflation Reduction Act in the U.S. provides up to \$3/kg H_2 , which has led to several project announcements for H_2 production using electrolyzers powered by low-carbon electricity [1–3]. Proposed electrolyzer projects include both “islanded” configurations, where renewable electricity is co-located with the electrolyzer and is the sole source of electricity input, as well as “grid-connected” systems involving using grid electricity (typically from the wholesale market) as well as on-site or contracted (via power purchase agreements) renewable electricity supply. In both cases, cost-effective operation of the electrolyzer will likely involve operating at much less than 100% capacity utilization to manage fluctuations in variable renewable energy (VRE) availability as well as grid electricity prices (that are also increasingly influenced by VRE availability) [4–8]. This part load operation not only has implications for capital utilization, which has been extensively studied, but also stack lifetime through accelerated degradation which is less well studied and could impact the overall economics of H_2 production [9–11]. Here, we focus on the answering this question in the context of grid-connected proton exchange membrane (PEM) electrolyzers.

As of 2022, global installations of electrolyzers totalled 700 MWe ¹, mostly composed of alkaline electrolyzers [12]. While the share of PEM electrolyzers is relatively small at 30% of total installed capacity, several appealing attributes compared to alkaline systems are expected to drive their deployment in the future [12]. In particular: a) their ability to operate at higher current densities ($\geq 1 \frac{\text{A}}{\text{cm}^2}$), which allows for smaller stack areas (and possibly lower areal footprint) to produce the same amount of H_2 , and b) ability to operate with a differential pressure between the anode and cathode, which enables production of high

¹Unlike many technologies, electrolyzer capacity is typically reported on the basis of nameplate electricity input rather than H_2 output

pressure H₂ product [12, 13]. The greater range of current density operation also creates the potential for increased operational flexibility which is an important criteria for cost-effective electrolyzer projects to manage fluctuations in temporal attributes, such as emissions or cost, of electricity supply [14–17]. The importance of such operational flexibility for power systems balancing is likely to grow with an increasing share of VRE supply in future low-carbon grids, owing increasing instances of near-zero prices and very high prices compared to today’s fossil-fuel dominant systems [18].

Several techno-economic optimization studies have highlighted the importance of dynamic operation in minimizing the operating cost of other electrochemical processes when utilizing electricity sourced from VRE that is co-located or supplied via connection to the electric grid [19–21]. Studies on PEM systems reveal that cost-optimal dynamic operation involves operating at high current densities (say $\gg 2 \frac{\text{A}}{\text{cm}^2}$) during times of abundant VRE supply or low electricity prices, as well as periods of idling or near-zero current densities during high electricity prices or low VRE supply periods, that collectively results in smaller stack areas when compared to an equivalent steady state electrolyzer operating at current densities near $1\text{-}2 \frac{\text{A}}{\text{cm}^2}$ [15, 16, 22–24].

Dynamic operation of PEM electrolyzers via modulation of the operating current density brings with it several challenges – namely, heat management, gas crossover and associated safety concerns, and stack degradation. Heat management in PEM systems is typically undertaken via excess feed water on the anode side [23, 25]. In an effort to model a 46 kWe electrolyzer connected to renewable energy, Espinosa et. al developed a model of the temperature response of PEM systems at varying current density with this excess feed water strategy [22]. With increasing current densities, the additional heat generated due to the higher overpotential will increase the water flow rates needed for heat management, and could create create implicit constraints on maximum current density levels. At the same time, in the absence of sufficient heat evacuation through increasing feed water flow rate,

the cell temperature could rise and begin vaporizing feed water as well as damage the membrane electrode assembly.

Another operational challenge of dynamic operation is hydrogen crossover to the anode under differential pressure operation, which represents both an energy loss and safety concern. The pressurized cathode provides a driving force for hydrogen to cross the membrane and mix with the oxygen at the anode. At 4% hydrogen in oxygen, the mixture reaches its lower flammability limit (LFL), presenting serious safety concerns. This crossover is generally greater under differential pressure operation and has been shown to be most problematic at low current densities when there is not enough oxygen production at the anode to keep the hydrogen concentration low [26]. While the crossover phenomenon has been well documented experimentally, most dynamic techno-economic models of PEM systems exclude any discussion of safety, crossover, or mitigation mechanisms (e.g. recombination catalyst on the anode side) [27, 28].

It is common for PEM systems to undergo degradation over time, which requires an increased voltage to the cell for the same current as a result of the increased high frequency resistances in the stack [29]. This degradation is a result of dissolution of catalyst, chemical degradation of the membrane, degradation of the bipolar plate, degradation of the current collector, and manufacturing defects [30, 31]. The industry standard model for PEM electrolysis techno-economics made by the National Renewable Energy Laboratory and U.S. Department of Energy assumes that the rate of degradation (increase in cell voltage) is independent of operation [32]. For electrolyzers operating statically (i.e. at constant current density), this constant rate of degradation may hold true. However, experimental studies have shown that degradation rate will be impacted by changes in operating current density [33–39]. To our knowledge, no techno-economic systems of PEMH₂ production systems account for this usage-based degradation though it plays a large roll in stack lifetime estimates and therefore replacement costs in these systems. Such operation-dependent degradation may alter the

incentives for dynamic operation and consequently impact the levelized cost of hydrogen (LCOH).

Our work seeks to address the above gaps in the techno-economic modeling of PEM electrolyzer systems. Our approach is based on a dynamic optimization framework that co-optimizes the design (stack area and on-site H₂ storage) and operation of the PEM electrolysis-based H₂ production process, with the following unique model elements: a) accounting for dynamic mass and energy balances at 15 min resolution at each electrode as well as flux across the membrane, b) development and use of an empirical correlation for characterizing degradation as a function of current density, which allows us to co-optimize stack replacement times, and c) accounting for safety and temperature related operational constraints and their impact on cost-optimal design and operation of the system. We use the model to investigate the cost-optimal sizing and operation of the PEM system under a range of electricity price scenarios representative of present low-VRE grids and future high-VRE penetration grids, as well as capital cost assumptions for the PEM electrolyzer. Through a systematic scenario-based framework, we isolate the impact of degradation on the levelized cost of hydrogen production. For instance, under 2022 capital cost assumptions for PEM systems, accounting for degradation could increase calculated LCOH by about 45% due to the use of larger stack sizes (2.3x) to minimize operation at high current densities (and hence degradation) and more frequent stack replacements (every 2 vs. 7 years) also due to degradation. Moreover, accounting for degradation after fixing the design of the system to that obtained without accounting for degradation could increase LCOH by a greater amount of 52%, which highlights the value of the proposed integrated design and scheduling (IDS) framework.

In general, scenarios that do not consider degradation tend to have a wider current density distribution, size larger H₂ storage, and utilize the electrolyzer more than scenarios that account for degradation. Applying the model to future electrolyzer capital cost and electricity price scenarios reveals several interesting findings. First, levelized costs are estimated around

\$2.50/kg dominated by cost of electricity and other fixed operating costs. Second, as stack costs decrease, the initially installed stack size increases, which further reduces instances of high current density operation and results in: a) increase time for stack replacement from 2 to 3-5 years depending on the electricity price scenario and CAPEX assumption and b) reduced capacity of installed H₂ storage (0.1 days of H₂ demand vs. 0.5 or greater in the 2022 scenarios).

Finally, we also investigated the impact of enforcing a safety constraint that limits H₂ build up in the anode to avoid an explosive mixture. We found that without this constraint, the electrolyzer’s cost-optimal operation profile tends to favor lower current densities which lowers the overall levelized cost but could result in H₂ concentration in anode exceeding 2% threshold and 4% LFL in a few periods.

2 Methods

2.1 Model Overview

In order to explore dynamic operation in the context of heat management, safety, and stack degradation, we develop a 0-D model of the electrolyzer process shown in Figure 1, which accounts for electrode-level mass balances, cell-level energy balances as well as electrochemical conversion described by the bottom-up characterization of the polarization curve. Below we provide a brief description of the model, with the complete mathematical description given in the supporting information (SI), along with the model nomenclature in Tables S1 - S3.

Figure 1 shows the process flow diagram for the electrolyzer and balance of plant which has been adapted from the literature and is consistent with industrial PEM installations [22, 25, 40]. Deionized water is pumped into the electrolyzer where the electrolytic reaction takes place. Gases and excess water leave in streams 3 and 4 and are sent to flash drums to separate the vapor from the liquid. It is assumed that a negligible amount of gas is dissolved in the

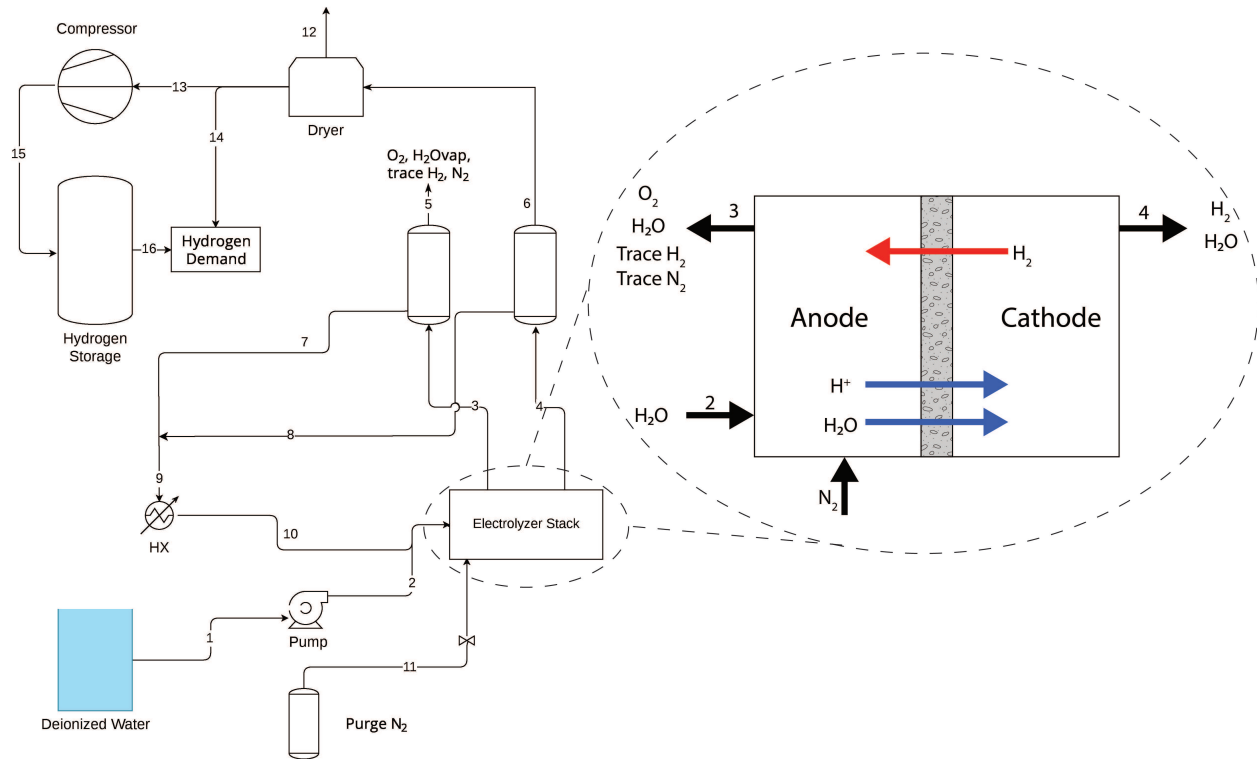


Figure 1: Flowsheet for the current work. Cell level details with flows across the membrane are shown in the cutout. Downstream treatment of the anode gas stream is not considered. The H₂ stream is dried and can either be compressed and stored to satisfy demand at a later time, or directly used to satisfy demand. Stream 11 is a nitrogen purge stream available for the model to use at a cost as a fail-safe should the concentration of H₂ in O₂ reach the 2% safety limit.

liquid water leaving the flash drum. Water from the flash drum is cooled and recycled back into the electrolyzer stack. The H₂ in stream 6 is dried and then either compressed into H₂ storage or used to satisfy the H₂ demand. Since the focus of the study is on H₂ production, the treatment of the anode gas stream, primarily composed of O₂, is not considered for this study. Stream 11 is a nitrogen purge stream that is modeled as a backstop to ensure H₂ concentration in the anode stays well below the lower flammability limit. This stream is only used as a fail safe to make sure an explosive mixture is not formed at the anode.

2.2 General Optimization Formulation

Given a fixed demand for H₂, the system as described and the model presented in the SI can be used to minimize the total cost of a PEM electrolyzer system. The general form for such an optimization is shown in Equation 1.

$$\begin{aligned}
 \min_{x,y} \quad & PV = C^{stack}(x) + C^{storage}(x) + C^{vOPEX}(x, y) \\
 \text{s.t.} \quad & f(x, y) = 0 \\
 & g(x, y) \leq 0 \\
 & x \in \mathbb{R}^n, y \in \mathbb{R}^m
 \end{aligned} \tag{1}$$

The objective function is the present value of the system which is a sum of the cost of the electrolyzer stack, C^{stack} , the cost of H₂ storage, $C^{storage}$, and the variable operating costs, C^{vOPEX} , which are primarily the cost of electricity and deionized water. The decision variables can be separated into two classes, x which represents the decision variables related to electrolyzer and storage sizing, and y , representing the time-dependent operational variables calculated from the relations in f and constraints represented by g . A detailed description of the optimization problem is presented in the following sections.

2.3 Reformulated Model

Rather than solve a single monolithic non-convex optimization model which is computationally challenging, we apply a decomposition strategy similar to Roh et. al and Chung et. al [16, 41]. This approach decouples the sizing of the electrolyzer (the outer problem) and the operational optimization given a fixed electrolyzer area and storage capacity (the inner problem) as illustrated in Figure 2 (explained in a later section).

2.3.1 Outer Problem

The outer problem iterates over the total number of cells in the electrolyzer set up, N_c , and number of days of H₂ storage $\Gamma_{H_2,stor}$. Each cell is assumed to have an area of 450 cm² represented by A_{cell} . The cost of the stack and storage can then be calculated as

$$C^{stack} = N_c A_{cell} p^{stack} + C^{mBoP} + C^{eBoP} \quad (2)$$

$$C^{storage} = \Gamma_{H_2,stor} \dot{m}_{H_2} p^{storage} \quad (3)$$

where C^{mBoP} mechanical balance of plant capital cost, C^{eBoP} , electrical balance of plant capital cost, p^{stack} is the capital cost of the stack in \$/cm², \dot{m}_{H_2} is the daily H₂ production rate in kilograms as calculated by the inner problem, and $p^{storage}$ is the cost of storage in \$/kg H₂.

$$C^{mBoP} = \alpha^{mBoP} \dot{m}_{H_2} \quad (4)$$

$$C^{eBoP} = \alpha^{eBoP} P^{max} \quad (5)$$

The mechanical and electrical balance of plant are scaled based on the rate of H₂ production

and peak power consumption for the facility, as shown in Equations 4 and 5. The mechanical balance of plant represents the compressors, pumps, DI water system, and H₂ separation system while the electrical balance of plant includes all electrical components necessary to make the interconnection to the grid including a rectifier. Here, α^{mBoP} is a cost factor in \$/kg H₂, α^{eBoP} is a cost factor in \$/kWe, and P^{max} is peak power consumption of the system in kWe as calculated by the inner problem. P_{max} is then a parameter passed to the outer problem to calculate the CAPEX for a given outer problem iteration.

2.3.2 Inner Problem

The inner problem takes a fixed N_c and $\Gamma_{H_2,stor}$ and minimizes operating cost while meeting the daily production target of $50,000 \frac{\text{kg}}{\text{d}}$. The inner problem can be written as a minimization of the operating cost as defined in Equation 6.

$$\begin{aligned}
\min_{\mathbf{x}} \quad & C^{vOPEX} = C^{elec} + C^{BoP,elec} + C^{water} + C^{N_2} \\
\text{s.t.} \quad & \text{electrochemical model, Equations S1 -S12} \\
& \text{mass balances, Equations S13-S26} \\
& \text{energy balance, Equations S27 - S31} \\
& \text{H}_2 \text{ storage constraints, Equation 17-22} \\
& \dot{m}_{H_2} \geq 50,000 \frac{\text{kg}}{\text{d}} \\
& 60^\circ\text{C} \leq T \leq 80^\circ\text{C} \\
& 0.1 \frac{\text{A}}{\text{cm}^2} \leq i \leq 4 \frac{\text{A}}{\text{cm}^2} \\
& y_{H_2,anode} \leq 0.02
\end{aligned} \tag{6}$$

where \mathbf{x} represents the primary decision variables, C^{elec} is the annual cost of electricity used by the electrolyzer, $C^{BoP,elec}$ is the annual cost of electricity consumed by the balance of plant, C^{water} is the annual cost of the deionized water, and C^{N_2} is the annual cost of the

nitrogen gas used at the anode for purging.

The model is subject to the mass and energy balances outlined in the SI as well as a demand constraint of $50,000 \frac{\text{kg}}{\text{d}}$ of H_2 . An operating temperature range of $60^\circ\text{C} - 80^\circ\text{C}$ was imposed on the stack. Additionally, a minimum and maximum current density were applied in this study. The minimum current density was chosen based on minimizing degradation at low voltages and the high current density was chosen based on the limit of commercialized PEM today [31]. In order to ensure 4% H_2 in O_2 at the anode is never reached a safety factor of 2 was applied making another constraint of a maximum of 2% H_2 in O_2 at the anode.

Evaluating each variable in the system for 15 minute time periods over the course of a year quickly becomes computationally intractable. To maintain computational tractability, we approximate annual operating costs through modeling operation over representative days at 15 min resolution assuming the hourly price of electricity holds for the entire hour. Time domain reduction using k-means clustering was performed for each electricity price time series data in order to find 7 representative days. Further details of the clustering method can be found in SI 5.2.

The clustering created a mapping $f : d \rightarrow r$. Each real day, d , is mapped to a representative day, r . To distinguish between variables for real or representative days, any variable with a bar above it is a variable that is indexed by the set of representative days.

Beginning with the cost of electricity for the electrolyzer,

$$C^{elec} = \sum_{d=1}^{365} C_d^{elec} \quad (7)$$

$$C_d^{elec} = \int_0^\tau p_d^{elec}(t) i_d(t) A \left(V_d^{undeg}(t) + V_d^{deg,cuml}(t) \right) dt \quad (8)$$

where τ represents the end of a representative day, p^{elec} represents the price of electricity, i is

the current density, $A = N_c A_{cell}$ is the total electrolyzer area, V^{undeg} is the voltage without considering degradation (based on polarization curve - see Equations S1 -S12), and $V^{deg,cuml}$ is the cumulative increase in voltage due to degradation.

The first term in the integral can be mapped to its respective representative day via $f(d) \rightarrow r$. However, the second term that accounts for the cumulative degradation that changes over the 365 day range and is inter-temporally coupled. So C_d^{elec} becomes:

$$C_d^{elec} = \int_0^\tau p_{f(d)}^{elec}(t) i_{f(d)}(t) A \left(V_{f(d)}^{undeg}(t) + V_d^{deg,cuml}(t) \right) dt \quad (9)$$

In accordance with the degradation correlation based on experiential literature values seen in Figure 4, we use the following model to represent the change in degradation over a representative day r :

$$\frac{d\bar{V}_{deg,r}}{dt} = \begin{cases} a & \bar{i}_r \leq 1 \\ a [\bar{i}_r(t)]^2 & \bar{i}_r > 1 \end{cases} \quad (10)$$

Cumulative degradation for real day d can then be written as

$$V_d^{deg,cuml}(t) = V_{d-1}^{deg,cuml}(t) + \delta\bar{V}_{f(d)}^{deg}(t) \quad (11)$$

where $\delta\bar{V}_{deg,f(d)}(t)$ comes from solving the differential equation in Equation 10 up to the time point of interest. Initial degradation at the beginning of the year for a fresh stack is assumed to be 0 V.

Using the mapping $f(d) \rightarrow r$, C_d^{elec} can be written

$$C_d^{elec} = \int_0^\tau \bar{p}_r^{elec}(t) \bar{i}_r(t) A \left(\bar{V}_r^{undeg}(t) + V_{d-1}^{deg,cuml}(t) + \delta\bar{V}_r^{deg}(t) \right) dt \quad (12)$$

The annual cost of electricity is then written:

$$C^{elec} = \sum_{r=1}^7 w_r \int_0^\tau \bar{p}_r^{elec}(t) \bar{i}_r(t) A (\bar{V}_r^{undeg}(t) + \delta \bar{V}_r^{deg}) dt + \sum_{d=1}^{365} \int_0^\tau \bar{p}_r^{elec}(t) \bar{i}_r(t) A V_{d-1}^{deg,cuml}(t) dt \quad (13)$$

where w_r represents the weight of representative day r as determined by the clustering.

$C^{BoP,elec}$, C^{water} , and C^{N_2} can be calculated in a similar manner using the associated representative days and mapping f .

$$C^{BoP,elec} = \sum_{r=1}^7 w_r \int_0^\tau [\alpha^{mBoP} \dot{m}_{H_2,r} \bar{p}_r^{elec}(t) + W^{compress} \bar{p}_r^{elec}(t)] dt \quad (14)$$

$$C^{water} = \sum_{r=1}^7 w_r \int_0^\tau [\dot{n}_{H_2O,consum,r} + \dot{n}_{H_2O,vap,5,r} + \dot{n}_{H_2O,vap,6,r}] p^{water} dt \quad (15)$$

$$C^{N_2} = \sum_{r=1}^7 w_r \int_0^\tau \dot{n}_{N_2,11,r} p^{N_2} dt \quad (16)$$

where $W^{compress}$ is the work of the H_2 storage compressor, p^{water} is the price of deionized water, and p^{N_2} is the price of nitrogen. Compressor work is evaluated using a single stage isentropic compression with an isentropic factor of 0.7 as outlined in Kahn et. al and Chung et. al [16, 42].

2.3.3 H_2 Storage

H_2 storage is necessary to enable meeting base load H_2 demand with flexible electrolyzer operation. We model the state of charge variation in H_2 storage considering both the short-term (intra-day) and long-term (inter-day) changes resulting from hour-to-hour discharging/charging activity. Following the method of Narayanan et. al [43] and Kotzur et. al [44], the storage state of charge variation throughout the year is approximated as as a super-

position of: a) inter-day state of charge variations modeled over all days of the year and b) intra-day state of charge variations modeled only for the representative days. This approach enables us to respect inter-temporally coupled nature of energy storage operations without the need to model all time periods of the year.

Long duration storage as well as intra-day storage are formulated as follows:

$$\delta_r = \bar{\Lambda}_r^{\text{H}_2, \text{stor}}(\tau) - \bar{\Lambda}_r^{\text{H}_2, \text{stor}}(0) \quad \forall r \in D_r \quad (17)$$

$$\Lambda_1^{\text{H}_2, \text{stor}}(0) = \Lambda_{365}^{\text{H}_2, \text{stor}}(\tau) + \delta_{f(365)} \quad (18)$$

$$\Lambda_{d+1}^{\text{H}_2, \text{stor}}(0) = \Lambda_d^{\text{H}_2, \text{stor}}(0) + \delta_{f(d)} \quad (19)$$

$$\Lambda_d^{\text{H}_2, \text{stor}}(0) = \bar{\Lambda}_r^{\text{H}_2, \text{stor}}(\tau) - \delta_{f(d)} \quad \forall d \in D \quad (20)$$

$$\frac{d\Lambda_d^{\text{H}_2, \text{stor}}}{dt} = \dot{n}_{15, f(d)}(t) - \dot{n}_{16, f(d)}(t) \quad (21)$$

$$\frac{d\bar{\Lambda}_r^{\text{H}_2, \text{stor}}}{dt} = \dot{n}_{15, r}(t) - \dot{n}_{16, r}(t) \quad (22)$$

$$\Gamma_{\text{H}_2, \text{stor}} \dot{m}_{\text{H}_2} \geq \max \left(\bar{\Lambda}_r^{\text{H}_2, \text{stor}}, \Lambda_d^{\text{H}_2, \text{stor}} \right) \quad (23)$$

where δ_r is the positive or negative change in storage levels that occurs over representative day r and allows for H_2 storage to carry over between representative periods. Equation 18 represents a wrapping constraint between the last day in the year and the first day in the year. Equation 19 allows H_2 storage to carry over between real days. Equation 20 relates the beginning of a real day of storage to the associated beginning of the representative day. Equations 21 - 22 ensure the mass balance across the H_2 storage is closed over real and representative days. Finally, Equation 23 ensures all storage state of charge variables are less than the maximum amount of H_2 storage. A visual representation of the storage formulation is included in the SI in Figure S1.

2.3.4 Implementation Approach

The outer and inner problems can be combined in an iterative manner using the algorithm described in Figure 2.

Upper and lower bounds for the electrolyzer area and number of days of H₂ storage are chosen based on physical limits of the electrolyzer in order to satisfy the 50,000 $\frac{\text{kg}}{\text{d}}$ H₂ demand. For this study, an area range of 40,000 – 300,000 450 cm² cells and a storage range of 0.1 – 14 days were chosen where one day of storage is equivalent to 50,000 kg of H₂. From the GSS algorithm two trial areas and two trial storages are chosen as is done by Sandhya et al assuming unimodality in each of the search directions [45]. This creates a total of four trial points in this 2D search space. The operational optimization is run for those 4 trial points which results in four different variable operating costs. For the PEM system, in the limit of very large electrolyzer areas, high capital costs would result in a high present value. In the limit of small areas, the system would need to operate at high current densities which would result in more stack replacement and a high present value. Storage also exhibits a similar unimodal trend at the extremes.

With the size of each system and the variable operating cost estimated, the present value for each of the four trial points can be calculated. If the trial areas and number of storage days are within the user defined tolerance (0.1% in this study), then the algorithm terminates and the final solution corresponds to the solution of trial point problems with the lowest present value. The variable operating routine from the associated minimum present value is then the optimal operation routine and the area and number of days of storage from the minimum present value are the optimal sizing of the system.

If still outside the tolerance, regions in the 2D space where the minimum cannot lie are eliminated. For example, for A and $\Gamma_{\text{H}_2,stor}$ where $A_{lb} \leq A \leq A_{ub}$ and $\Gamma_{\text{H}_2,stor,lb} \leq \Gamma_{\text{H}_2,stor} \leq \Gamma_{\text{H}_2,stor,ub}$ and given four present values that are functions of the two trial areas and two trial storages $PV_A(A_1, \Gamma_{\text{H}_2,stor,1})$, $PV_B(A_2, \Gamma_{\text{H}_2,stor,1})$, $PV_C(A_1, \Gamma_{\text{H}_2,stor,2})$, $PV_D(A_2, \Gamma_{\text{H}_2,stor,2})$, we can

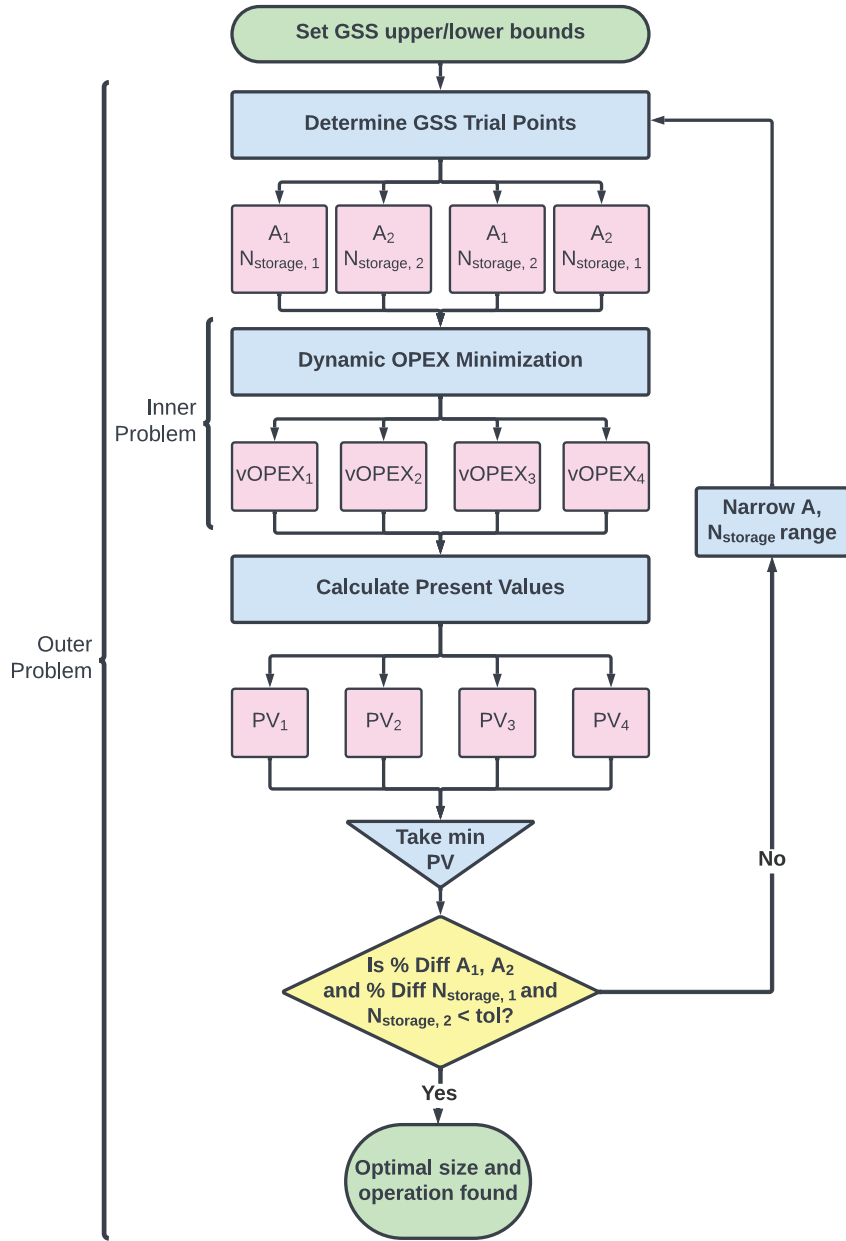


Figure 2: Summary of the bilevel optimization. The outer problem iterates over number of cells and H_2 storage capacity. The inner problem solves the cost optimal variable operation problem given a fixed number of cells and storage from the outer problem.

eliminate a portion of the search region by finding the minimum of the present values. If PV_A is the smallest present value, we know the minimum will not lie in $A_2 \leq A \leq A_{ub}$ and $\Gamma_{H_2,stor,2} \leq \Gamma_{H_2,stor} \leq \Gamma_{H_2,stor,ub}$. Thus A_2 and $\Gamma_{H_2,stor,2}$ become the new upper bounds. Similar eliminations can be made if the smallest present value is one of the other three values. The algorithm repeats until converged on a locally optimal solution. Due to the non-linearity of the problem, a global optimum is not guaranteed.

The NLP to solve the operational problem was implemented in Python using Pyomo, specifically Pyomo DAE with IPOPT as the non-linear solver [46, 47]. Linear solver MA86 was chosen to use in IPOPT for its ability to handle large problems well [48]. The bilevel optimization approach with the degradation correlation results in a problem with $\approx 200,000$ continuous variables, $\approx 200,000$ equality constraints, and $\approx 2,500$ inequality constraints. Full details of each run can be found in Table 2 and in the SI in Table S4. The problem was run using resources on MIT’s SuperCloud HPC [49].

Table S5 shows how the bi-level optimization approach scales with the number of representative days. As we increase the number of representative days we expect convergence to a value for storage, number of cells, and LCOH, although this will not be monotonic due to the different effect of each added day to the optimization. Although increasing number of representative days allows for capturing greater day-to-day variability in the underlying electricity price time series, it increases the overall problem size and the computational burden as indicated by the time to convergence and avg. run time per GSS iteration. We choose 7 representative days to strike a balance between computational tractability and accuracy.

2.4 Data Inputs

2.4.1 Techno-economic Data

For the 2022 case, capital and operating cost assumptions were made consistent with the 2019 version of NREL’s H2A model adjusting for inflation from 2019 to 2022 [32]. The 2030

Table 1: Techno-economic parameters for model. Consistent with NREL’s H2A Model, Chung et. al, and Fraunhofer ISE [16, 25, 32]. Planned replacement costs are used as the stack replacement cost when a replacement is necessary.

Techno-economic Parameter	2022	2030	Units
Stack CAPEX	\$2.37	\$0.79	\$/cm ²
BoP CAPEX	289	103	\$/kWe
Storage CAPEX	\$500	\$300	\$/kg H ₂
Site Prep	2%		of direct capital
Engineering	10%		of direct capital
Contingency	15%		of direct capital
Permitting	15%		of direct capital
Planned Replacement	15%		of direct capital
Unplanned Replacement	0.5%		of direct capital
Overhead	20%		of labor cost
Tax/Insurance	2%		of total CAPEX
BoP Electricity Usage	5.1		kWh/kg H ₂

case capital costs come from Fraunhofer ISE’s cost forecast for PEM and alkaline electrolysis [25]. Summary of the cost assumptions can be found in Table 1.

Using the parameters in Table 1, capital cost ($C^{CAPEX} = C^{stack} + C^{storage}$), unplanned replacement costs (C^{UPR}), planned replacement costs (C^{PR}), fixed operating cost (C^{fOPEX}), and variable operating cost (C^{vOPEX}) can be estimated. Assuming a plant life of 40 years and a discount rate of 8%, the present value of the project (PV) can be estimated as shown in Equation 24.

$$PV = C^{stack} + C^{storage} + \sum_{y=1}^{40} [C^{UPR} + C^{PR} + C^{fOPEX} + C^{vOPEX}] \frac{1}{(1+d)^y} \quad (24)$$

The direct capital needed to calculate the above costs is the sum of the cost of the stack and cost of the balance of plant. For the scenario run without useage-dependent stack degradation, the replacement rate for the stack was fixed at 7 years [32]. For the scenarios where degradation is accounted for as shown in Equation 10, a degradation rate-informed replacement rate is calculated as follows. Based on the fixed H2A degradation rate, approximately

$\Delta_{deg}^{max} \approx 1V$ of degradation is allowed to occur before the stack needs to be replaced [32]. The operational optimization of the problem gives the degradation of a fresh stack after one year of operation (Δ_{deg}^1). The replacement rate can then be defined as:

$$r_{stack} = \begin{cases} \left\lfloor \frac{\Delta_{deg}^{max}}{\Delta_{deg}^1} \right\rfloor & \Delta_{deg}^1 \leq 1 \\ 1 & \Delta_{deg}^1 > 1 \end{cases} \quad (25)$$

For implementation purposes, if the degradation of the stack exceeds 1 V in a given year, the stack is allowed to run until the end of the year before being replaced.

Fixed operating cost is the sum of the cost of labor, overhead, tax and insurance, and material. The labor rate was assumed to be \$70 per hour per worker where 10 workers are needed for a system of this size, and the plant is assumed to operate 350 days per year.

Variable operating cost for the first year is simply obtained from the objective function of the operational optimization. Post-convergence of the operational optimization, the variable operating cost is updated to include degradation for the years leading up to replacement. This assumes that degradation in each future year is the same as the first year after stack replacement.

The amount of H_2 produced in one year (M_{H_2}) can be discounted in a similar way as the present value of the project as seen in Equation 26. The levelized cost of H_2 is then calculated as the ratio of the two present values.

$$PV_{H_2} = \sum_{y=1}^{40} \frac{M_{H_2}}{(1+d)^y} \quad (26)$$

$$LCOH = \frac{PV}{PV_{H_2}} \quad (27)$$

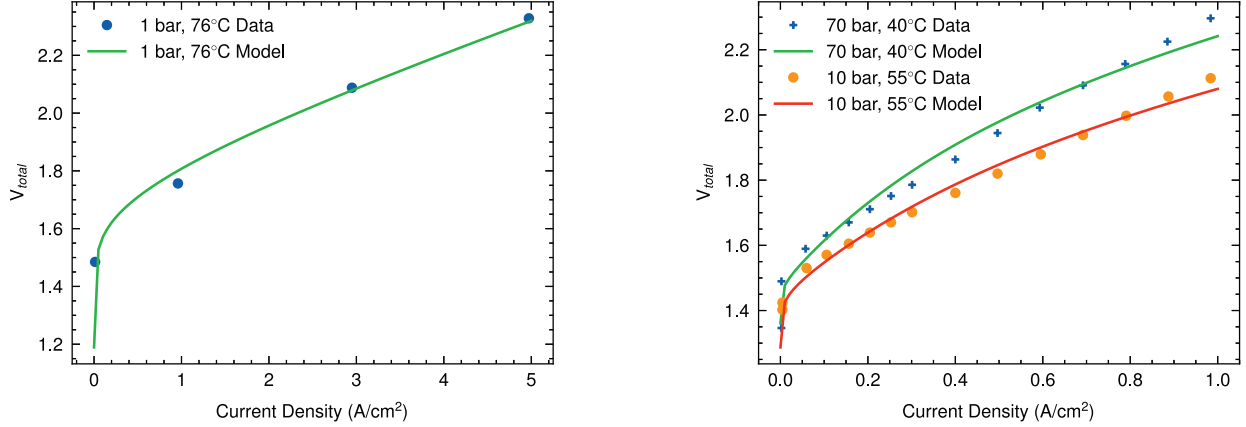


Figure 3: Left Figure: Current voltage relationship at 1 bar and 76°C. Data from [50]. Fitted parameters $\alpha_{an} = 0.58$, $\alpha_{cat} = 1.28$. Right Figure: Current voltage relationship at high pressure. Data from [51]. Fitted parameters at 40°C: $\alpha_{an} = 1.9$, $\alpha_{cat} = 0.1$, fitted parameters at 55°C: $\alpha_{an} = 1.38$, $\alpha_{cat} = 0.11$

2.4.2 Electrolyzer Performance and Model Assumptions

Validation of the electrochemical model without degradation at different temperatures and operating pressures is shown in Figure 3. The model fits well across varying current densities, pressures, and temperatures.

Many degradation studies have been done on PEM cells that attempt to characterize the degradation rate of the cell as a function of the applied current density [33–37, 39]. We use data from these studies to construct a usage-based degradation rate. The operating current density and degradation rate have been averaged over the lifetime of the cell and only square and hold wave patterns were taken from the degradation studies [33–37, 39]. Additionally some studies exhibited a negative degradation rate likely to a decrease in ohmic losses from membrane thinning. For this work, those data points were not considered.

Figure 4 illustrates the points taken from literature, and Equation 28 shows the correlation found. The degradation rate increases linearly with the square of the current density for $i > 1 \frac{A}{cm^2}$. The experiments at low current density do not follow this linear trend but instead have a relatively constant degradation rate. The degradation rate was thus modeled as a

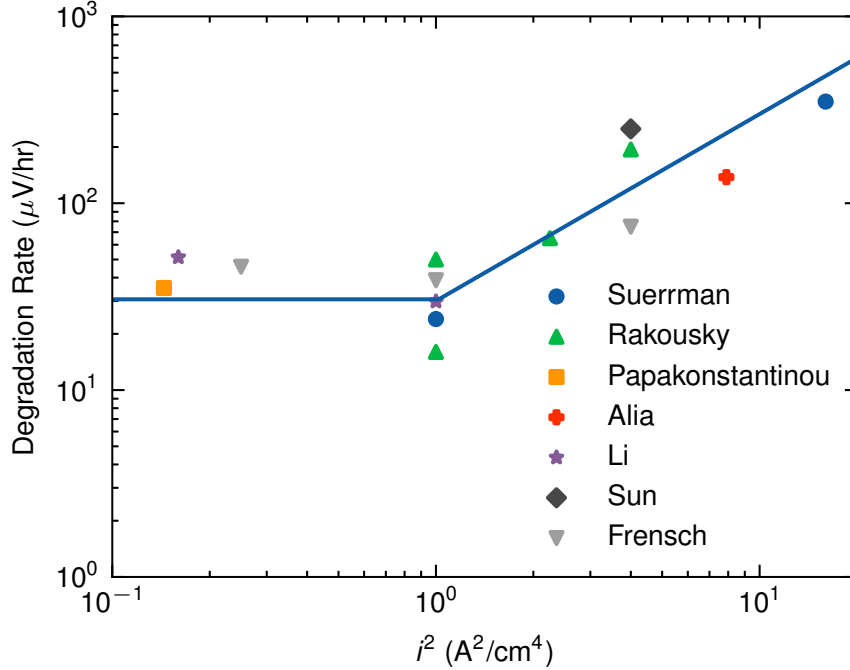


Figure 4: Degradation rate as a function of the square of the current density plotted on a log-log axis. Data taken from [33–37, 39]. Current density and degradation are time averaged over the operation lifetime. Points shown in the graph here are for square and hold wave patterns. Some cells showed negative degradation rates likely due to membrane thinning; these negative degradation rates were not considered for this study.

piece-wise function shown in Equation 28. The constant in the equation is a fitted parameter from the data.

Pushing electrolyzers to higher and higher current densities past the $4 \frac{\text{A}}{\text{cm}^2}$ maximum presented in this work makes the economics more favorable when degradation is ignored [16]. Bench scale experimentalists have already begun to push up to $10 \frac{\text{A}}{\text{cm}^2}$ [52]. However, operating at higher and higher current densities could potentially result in increased degradation rates if one assumes the extrapolation of the trend in Figure 4.

$$\frac{dV_{deg}}{dt} = \begin{cases} 30 & i \leq 1 \\ 30 [i(t)]^2 & i > 1 \end{cases} \quad (28)$$

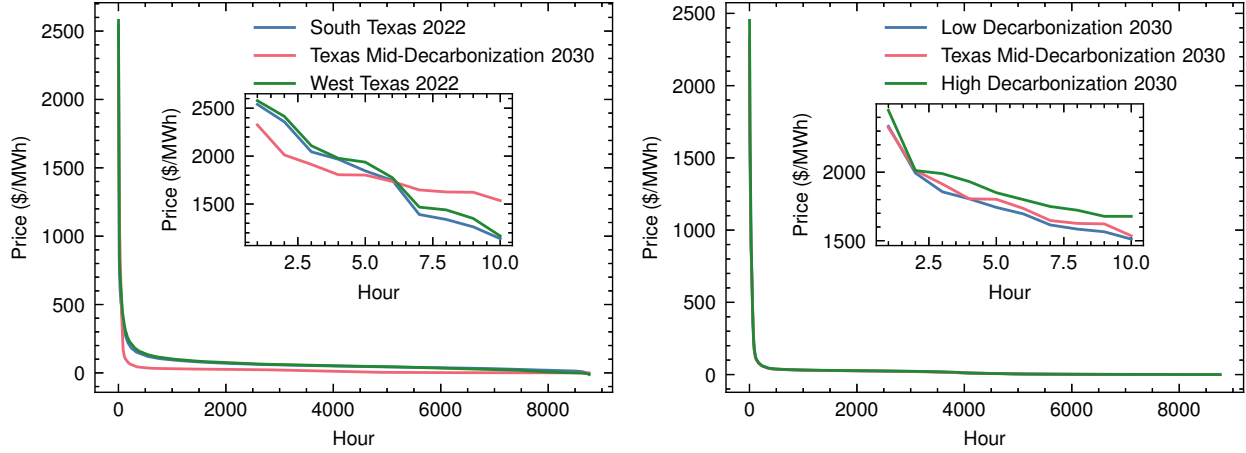


Figure 5: Left Figure: Duration curves for 2022 and 2030 prices used in this study. The south load zone (avg. price: \$62.55) and west load zone (avg. price: \$63.83) prices are for 2022. The 2030 case is the mid-case for NREL’s Cambium model for 2030 Texas (avg. price: \$21.43). Right Figure: Duration curves for 2030 prices used in this study. The low decarbonization scenario projects 95% decarbonization of the grid by 2050 (avg. price: \$21.97). The high decarbonization scenario projects 100% decarbonization of the grid by 2030 (avg. price: \$22.67).

2.4.3 Electricity Price Scenarios

Corpus Christi, Texas was used as a case study for this work due to its proximity to existing H_2 demand from the petrochemical sector on the Texas Gulf coast which has prompted commercial interest to deploy GW-scale electrolyzers in that region [3]. In order to consider the impact of current and future electricity price scenarios, historical electricity prices from the years 2022 and price projections available for 2030 were used. Electricity prices were taken from 2022 ERCOT South load zone historical pricing [53]. For the 2030 scenario, prices were taken from NREL’s Cambium future electricity prices model mid-case for Texas [54]. These projected future prices represent a moderately decarbonized grid by 2030. Prices are shown in the left panel of Figure 5. The average electricity price is higher in 2022 than in 2030. However the 2030 price scenario exhibits more volatile prices.

In order to show the model’s sensitivity to 2022 electricity prices, a case with electricity prices from the West Texas load zone in 2022 (another location with many planned elec-

trollyzer projects) was run. For sensitivity to 2030 electricity prices, the Cambium model gives a scenario where the grid is 100% decarbonized by 2030 (high decarbonization) and 95% decarbonized by 2050 (low decarbonization). The duration curves for these price series in comparison to the mid-case are shown in the right panel of Figure 5.

2.4.4 Limitations of Model

While this model accounts for many of the aspects of dynamic operation including usage-based degradation, it does have some limitations. In this work we solve a non-linear, non-convex optimization with a local solver IPOPT. There is no guarantee we have converged on the global solution, so a lower cost solution could exist. However, any local minimum will be better than operating naively or statically and a global solution is not strictly necessary in practice.

Additionally, we model the economics of the system as a price-taker. In other words, we must accept the price of electricity, and our operation has no influence on the prices of electricity. In reality, especially with increasing demand on the grid for electrified industrial processes, dynamic operation to best utilize cheap electricity prices would influence the local cost of electricity, as shown by other studies [17, 55].

3 Results and Discussion

In order to demonstrate the sensitivity of the model to capital cost assumptions, electricity price assumptions, and other constraint assumptions, various test cases were run. All scenarios contain the degradation correlation unless “no use-dependent degradation” is indicated. Capacity factor for the scenarios is calculated by taking the ratio of the energy actually used by the system and the energy used by the system if it were to operate at the maximum current density of $4 \frac{\text{A}}{\text{cm}^2}$. A summary of the tests run with high level results are in Table 2.

Table 2: High level results of electrolyzer design and scheduling optimization. One day of storage is defined as 50,000 kg of H₂. Replacement rate is defined as the maximum degradation allowed (1 V) divided by the degradation after 1 year. Annual electrolyzer utilization defined based on maximum current density operation for the 350 working days of the year considered in this model. Convergence time is reported in Table S4.

Case	Price Series	Total CAPEX (in thousands)	vOPEX (in thousands)	LCOH (\$/kg)	Days of Storage	Number of Cells (in thousands)	Degradation after 1 Year	Replacement Rate (Years)	Utilization
Degradation 2022 Case	2022, South LZ	\$ 366,800	\$ 45,400	\$ 6.60	0.51	116.2	0.45	2.2	25.8%
No Use-Dependent Degradation	2022, South LZ	\$ 203,900	\$ 50,900	\$ 4.56	1.39	50.1	–	7	70.1%
Degradation, West Texas	2022, West LZ	\$ 430,800	\$ 46,700	\$ 7.08	0.82	141.8	0.31	3.2	20.5%
Degradation, Fixed CAPEX	2022, South LZ	\$ 239,100	\$ 67,300	\$ 6.92	1.39	50.1	1.97	1.0	67.5%
High Temperature	2022, South LZ	\$ 362,000	\$ 45,600	\$ 6.56	0.84	110.5	0.50	2.0	27.0%
No Safety Constraint, Fixed CAPEX	2022, South LZ	\$ 315,200	\$ 47,500	\$ 6.21	0.51	116.2	0.41	2.4	25.2%
Degradation 2030 Mid-Case	2030, Texas Mid	\$ 200,000	\$ 9,400	\$ 2.47	0.20	156.8	0.25	4.0	18.2%
2030 High CAPEX	2030, Texas Mid	\$ 238,300	\$ 9,400	\$ 2.76	0.65	159.1	0.24	4.1	18.1%
2030 Low CAPEX	2030, Texas Mid	\$ 181,900	\$ 9,400	\$ 2.28	0.11	177.8	0.19	5.1	15.8%
2030 High Decarbonization	2030, Texas High	\$ 202,300	\$ 9,400	\$ 2.48	0.13	161.3	0.25	4.0	17.8%
2030 Low Decarbonization	2030, Texas Low	\$ 180,400	\$ 11,400	\$ 2.50	0.11	132.1	0.33	3.0	22.1%

Degradation vs No Use-Dependent Degradation

Figure 6 highlights the operational impact of incorporating current density dependent degradation in the techno-economic optimization model. Both scenarios produce optimal operating routines that ramp up current density (and therefore production of H_2) during periods of low prices and switch to idling at $0.1 \frac{\text{A}}{\text{cm}^2}$ (the minimum assumed current density) during periods of high electricity prices [31]. However, because the model with degradation is penalized by accumulating degradation, it operates at much lower current densities in order to minimize the cost of electricity while meeting the demand constraint of $50,000 \frac{\text{kg}}{\text{d}}$ of H_2 . When electricity prices start to rise, both models switch to the idling state.

The overall effect of degradation on the operation profile can be seen from the current density distribution in Figure 7. The accumulating degradation causes an increased power demand which forces the model with degradation to favor lower current densities on average, including idling as much as possible while meeting the demand constraint. The net result is that electrolyzer stack utilization (or capacity factor) with degradation is 26% as compared to 70% in the case without degradation.

Additionally, due to the increased overpotential from degradation, the case that accounts for degradation operates for more many more hours at the maximum temperature limit than the case without degradation. This is for two reasons: 1) the increased overpotential generates more heat in the system and would result in a higher temperature for the same inlet water flowrate, and 2) operating at a higher temperature lowers the activation and ohmic overpotentials of the cell that partially offset the impact of degradation.

Given today's electricity prices and capital costs for the electrolyzer stack, accounting for degradation results in a 45% higher LCOH than when use-dependent degradation of the stack is ignored (see Figure 9). The case with no use-dependent degradation has a LCOH that agrees well with the work done by Chung et. al although our model accounts for crossover, static degradation, and the energy balance over the stack [16]. The case without

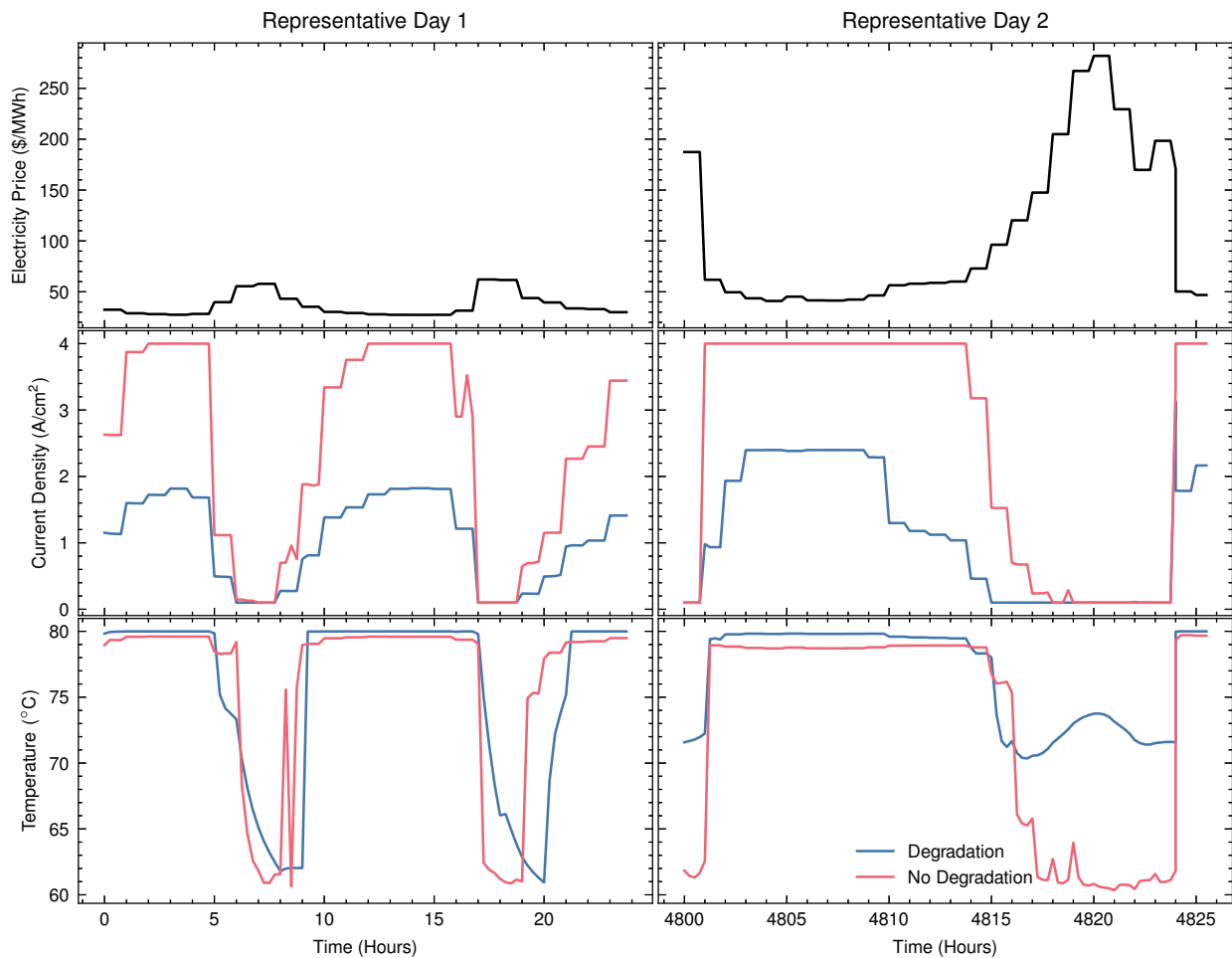


Figure 6: Impact of modeling use-dependent degradation on optimal electrolyzer operation and temperature profile. Results correspond to 2022 ERCOT South Load Zone price scenario. Two representative days, one from early in the year and one from late in the year, of operation are shown. In general, the case with degradation operates at lower current densities than the case without degradation. During the highest price periods of the day both cases idle at $0.1 \frac{\text{A}}{\text{cm}^2}$.

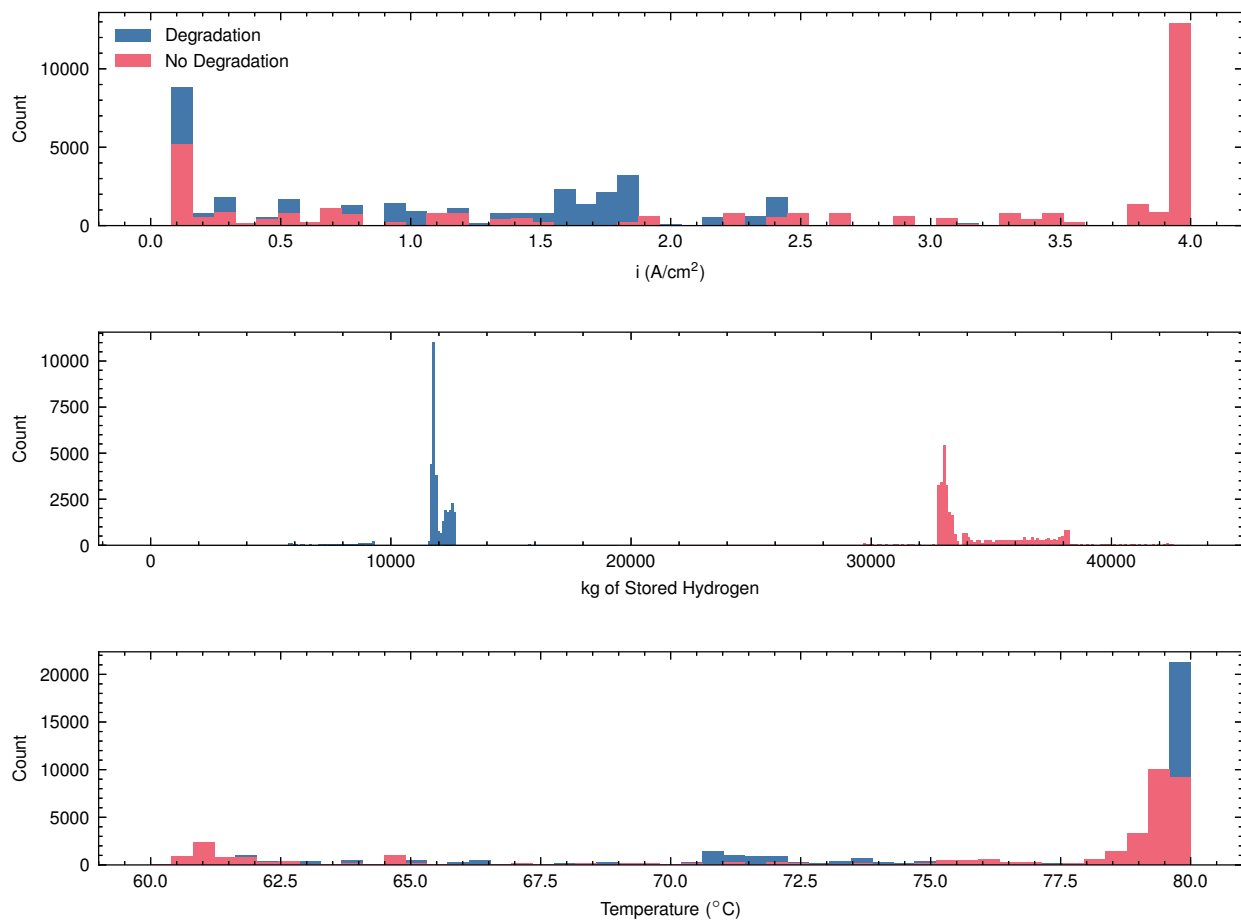


Figure 7: Cost-optimal current density, storage, and temperature distributions for the cases with and without use-dependent degradation. Accounting for degradation moves the distribution leftwards towards lower average current densities. Results corresponds to model optimization based on 2022 ERCOT South Load Zone scenarios.

use-dependent degradation also sized 2.7 times more H₂ storage than the case with it. Intuitively, when use-dependent degradation is not accounted for, the model is incentivized to maximize current density (and production) during periods of low electricity prices and turn down production during periods of high prices. This "bang-bang" operating pattern results in larger need for energy storage. With degradation, there is a reduced incentive for operating at high current densities and thus storage requirements are lower. Overall use-dependent degradation results in an overpotential of 0.45 V/year that shortens stack replacement to 2.2 years vs. 7 years without modeling use-dependent degradation. A second location in West Texas was also run to show this dynamic operation approach works in more than one electricity market (see Table 2).

To demonstrate the value of the IDS optimization approach, we ran an operational optimization with use-dependent degradation using the size of stacks and storage from the no use-dependent degradation case. The operational profile can be seen in Figure S4. In this highly constrained scenario, the model with degradation is forced to operate at higher current densities much like the case without degradation. Yet the effect of degradation is seen by the model avoiding operation at maximum current density of 4 A/cm². As a result, the system accumulates 1.97 V of degradation in one year. Consequently, stacks need to be replaced every year at the end of the year. This increases the levelized cost to \$6.92/kg which is a 4.6% increase over the case with degradation and a 52% increase over the case without usage-based degradation.

To test the sensitivity of the levelized cost on the degradation correlation and the replacement voltage threshold, two other sensitivity cases were run and compared with the 2022 degradation case: one where the coefficient in Equation 28 is reduced by half to 15 and one where the maximum allowed replacement threshold voltage is decreased from 1 V to 0.5 V. Results from these runs are summarized in Figure S2. Reducing the degradation correlation coefficient results in a 5.2% decrease in LCOH due to the longer lifetime of these cells (3.04

years), reducing the planned replacement costs. Reducing the replacement threshold voltage results in an 8.5% increase in LCOH mainly due to more frequent stack replacement (every 2.00 years) due to the lower threshold. Additionally, as seen in Figure S3, changes in the underlying degradation assumptions do influence operation as well. When the coefficient is lowered to 15, the model can operate at higher current densities than the base case. However, when the voltage threshold is lowered, the model must operate at lower current densities to keep degradation (and therefore replacement rate) low.

Impact of Higher Temperature

Since the temperature limit was a binding constraint, particularly with use-dependent degradation (Figure 6), we ran a scenario where the upper bound for the temperature of the cell was increased from 80°C to 90°C. The purpose of altering this was to determine if the upper bound of the temperature constraint included in the model was binding. As seen in Figure S5, operation of the system with the higher temperature bound marginally increases the current density during periods of low electricity prices. This is due to the fact that operating at a higher temperature lowers both activation overpotentials and ohmic overpotentials, which reduces operating costs and incentivizes higher current density operation (see Figure 3). For example, at $1 \frac{\text{A}}{\text{cm}^2}$ and 60°C the voltage is 1.78 V and at $1 \frac{\text{A}}{\text{cm}^2}$ and 80°C the voltage is 1.7 V.

When looking at the distribution of operating current densities over the year shown in Figure S6, it is clear the higher temperature upper bound case operates at slightly higher current densities generally. These hours of higher current density operation can take advantage of the extra H₂ storage sized in the high temperature upper limit case (See Table 2). The smaller number of cells in the high temperature upper bound case combined with a greater use of storage results in a \$0.04/kg lower LCOH when compared with the 2022 degradation case (see Figure 9). However, higher current density operation results in more degradation and a more frequent stack replacement rate of 2 years in comparison to the base case replacement

rate of 2.2 years (See Table 2).

Impact of Recombination Catalyst and Safety Constraint

Industrial PEM membranes come embedded with a gas recombination catalyst on the anode side [27, 28]. This catalyst lowers the concentration of H_2 at the anode by reacting the H_2 with oxygen to form water. In the original base model, we included a safety constraint. However, in practice, it may be difficult to enforce a safety constraint implying that the recombination catalyst might be the primary mitigation strategy. To evaluate whether the catalyst with 90% conversion is sufficient to ensure safe operation, we ran the model with the area and storage fixed from the cost-optimal base case with the catalyst present but without a safety constraint. Results are summarized in Figures S7 and S8.

The distribution of current densities with the relaxed safety constraint shifts to lower current densities. Intuitively, with the constraint relaxed, the model does not need to keep production of O_2 at the anode high and regardless of the rate of crossover can operate in the most cost optimal manner. Relaxation of the safety constraint results in a lowered levelized cost of \$6.21/kg. Though the levelized cost is lower, the H_2 lost to crossover increases from 11,300 kg/year in the base case to 30,400 kg/year in the case without a safety constraint, nearly a 3x change. This H_2 represents lost product as it is not recovered. Replacement rate increases slightly from 2.2 years to 2.4 years due to lower current density operation without the safety constraint, further contributing to the decrease in LCOH.

More important than the change in LCOH is the change in safe operating conditions. Without the safety constraint and with the recombination catalyst, the model exceeds the LFL of 4% at 1% of the time points. While only a small percentage of the time operating, crossing into the flammability region of the mixture of gases presents a serious safety concern with dynamic operation. In practice, the composition of the outlet gas of the anode should be monitored continuously. This composition measurement could potentially be integrated into

a controller that varies the flowrate of N_2 into the anode to keep H_2 concentrations well below the LFL.

Future Electricity Prices and Future CAPEX

To test the sensitivity of these results to future electricity prices and capital costs, we evaluated the model based on a representative 2030 electricity price scenario for Texas and three possible capital cost projections. Capital cost projections in the mid-range case are $\$0.79/\text{cm}^2$, consistent with Fraunhofer ISE [25]. The low capital cost case is $\$0.39/\text{cm}^2$, and the high capital cost case is $\$1.00/\text{cm}^2$.

The operational profile in Figure 8, shows that the 2030 mid-range CAPEX and high CAPEX case operate at similar current densities due to their similarly sized stacks and storage (see Table 2). Due to the increased cost of stacks in the high CAPEX case, the LCOH is 12% more than the mid-case (see Figure 9). For the lowest capital cost scenario, the number of cells increases by 13% and the amount of storage decreases by 47% compared to the mid-range case. With the greater number of cells, the scenario with the lowest capital cost can operate at lower current densities to avoid high degradation rates and keep operating costs lower. This results in a 7.7% decrease in LCOH from the mid-range case.

In order to test sensitivity to future electricity prices, another two scenarios with differing electricity prices were run with the mid-range capital costs scenario as shown in Figure 5. Figure S10 shows the differences in operation for the three different electricity price scenarios: the mid-decarbonization case, low decarbonization, and high decarbonization. While we do see the lowest decarbonization case able to operate at higher current densities, and a much larger sized storage for the high decarbonization case, ultimately, the LCOH is quite similar between scenarios indicating a weak relationship between LCOH and electricity price for this particular location (see Figure 9).

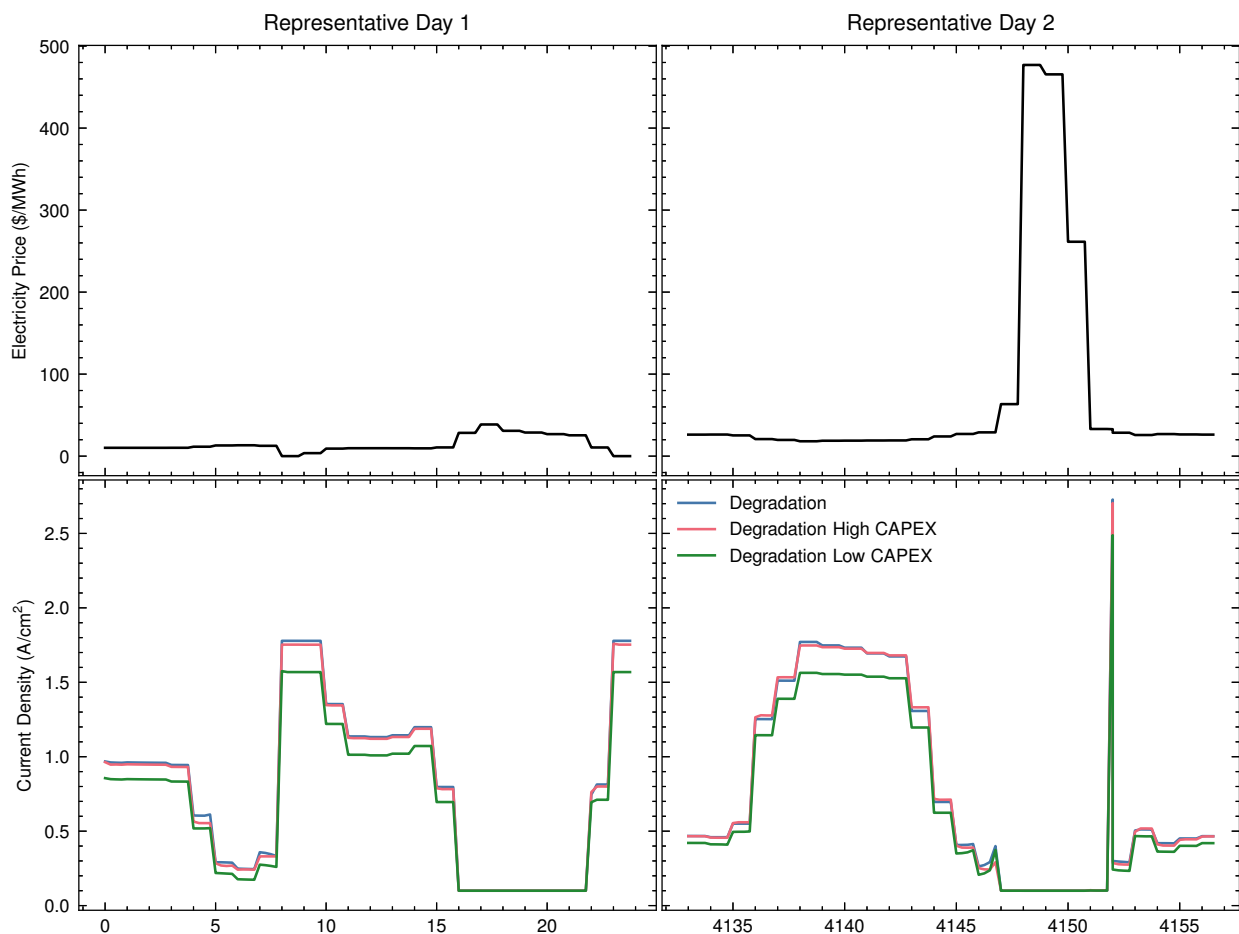


Figure 8: Two representative days with projected 2030 prices and projected 2030 capital costs. The mid-range CAPEX case has a stack CAPEX of \$ 0.79/cm², the high CAPEX case is \$1.00/cm², and the low CAPEX case is \$0.39/cm². The two cases with the higher capital costs operate quite similarly. The case with the lowest capital cost sizes many more cells and is able to therefore operate at lower current densities. Temperature profile included in Figure S9.

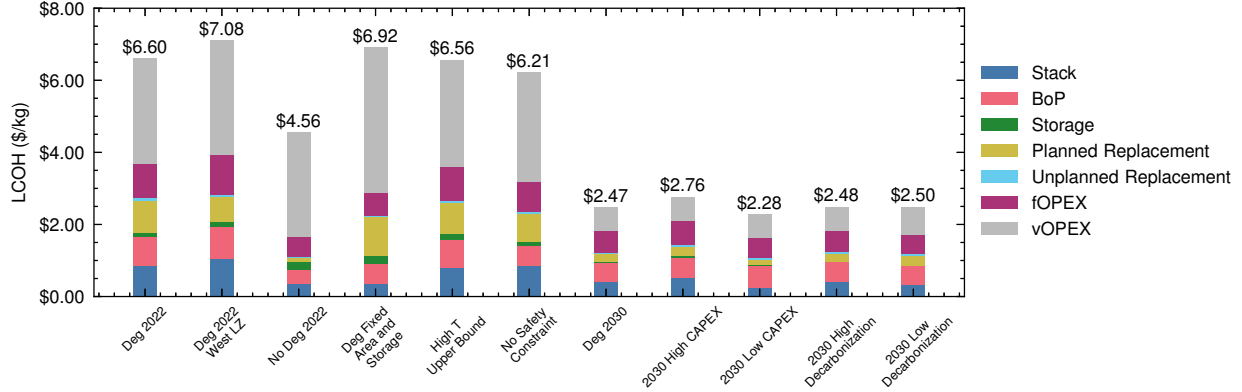


Figure 9: Levelized cost of H₂ for each of the cases. CAPEX Total is the capital cost of the stacks and downstream equipment, Planned Replacement is the cost for planned replacements of the stack as they age, Unplanned Replacement is the unplanned replacement cost as defined in Table 1, foPEX is the fixed operating cost, and vOPEX is the variable operating cost which is the cost of electricity and the cost of water used to feed and cool the stacks. Scenarios reported here are the same as reported in Table 2.

4 Conclusion

We developed a techno-economic optimization model for integrated design and scheduling of a PEM electrolyzer that respects temperature constraints, safety constraints, and models degradation of the electrolyzer stack as a function of its use. The model relies on an empirical correlation linking current density with degradation rate derived from experimental data in the literature, and is solved to co-optimize electrolyzer stack, balance of plant and storage capacity along with their operation. To enable computational tractability we employ number of techniques including approximating annual operations via operations over representative days, as well as 2-D GSS search algorithm that decomposes the investment and scheduling operating facilitates identification of locally optimal solutions of the resulting optimization model. We applied the model to explore the techno-economics of such a system and calculate the LOCH for various operating scenarios including current and future prices of electricity and stack capital costs.

Dynamic operation overall results in binding constraints on both temperature and safety limits. Heat management and safety of PEM systems must continue to be an area of focus

for the operators of PEM systems if dynamic operation is to be successfully implemented. The monitoring and manipulation of stack temperature and anode gas composition will require detailed process control.

Using the correlation outlined in this work, accounting for degradation resulted in a ≈ 2 year stack lifetime in comparison to the 7 year assumed lifetime in the 2022 scenario. The increase in stack replacement frequency could potentially increase the materials burden on critical minerals like Ir, unless recycling becomes commonplace. Previous works have highlighted the scarcity of Ir especially when considering aggressive decarbonization scenarios [56, 57]. The increased replacement frequency associated with dynamic operation could exacerbate this issue even with replacement rates projected to increase to ≈ 4 years by 2030. While some experimental work has begun to address this issue, significant advancements in PEM electrolyzer efficiencies, a decrease in Ir loadings in PEM, and a focus on PEM catalyst recycling are critical going forward [58].

The LCOH is higher in the 2022 case with degradation when compared to running without degradation. This indicates an underestimation of LCOH when operating dynamically in models that do not account for use-dependent degradation. We also show that optimizing design without accounting for use-dependent degradation and subsequently incurring these degradation costs leads to 4.6% higher LCOH than co-optimized design and operations case. Additionally, not accounting for stack degradation leads to an over-sizing in hydrogen storage.

Dynamic operation does indeed make more cost effective hydrogen under present cost scenarios, and we show that dynamic operation makes even more sense under future electricity and capital cost scenarios by significantly minimizing the variable operating cost of electricity (see Figure 9).

While the results presented in this paper highlight issues with cost optimal design and operation of PEM electrolyzers, there are some limitations to this analysis. Our work sought

to capture degradation behavior of PEM stacks, however, the degradation correlation was found using the limited data available in literature. Standard procedures for accelerated degradation of cells are needed in order to gather reliable data that then can be used in models. More in depth degradation studies that not only look at the effect of operating current density but also temperature and catalyst loading effects are needed. One other weakness of our approach is the fact that we solve a non-convex NLP with no guarantee of finding a global minimum. Indeed for a problem of this size, it could be expected that there would be multiple minima in the design and operation space.

Most importantly, the framework presented here to evaluate PEM electrolysis and hydrogen production can be applied to the design of other electricity-intensive processes. With growing interest in electrochemical/electricity driven processes, model set up and system design can be readily adapted to study other processes and systems. This framework can help quickly and effectively evaluate different processes on the basis of their economics while modeling the underlying physical phenomenon and dynamics.

Acknowledgements

The authors would like to acknowledge Edward Graham for his insightful contributions to this work. Funding for this work was provided by Analog Devices Inc.

Data Availability Statement

The model and data used to produce all figures and results will be provided upon reasonable request.

References

- [1] John Yarmuth. *Inflation Reduction Act*. Sept. 2021.
- [2] *Regional Clean Hydrogen Hubs Selections for award negotiations*. en. <https://www.energy.gov/oced>. Accessed: 2023-10-16.
- [3] Vanessa Arjona. *DOE Hydrogen Program Record*. Tech. rep. U.S. Department of Energy, June 2023.
- [4] John Stansberry, Alejandra Hormaza Mejia, Li Zhao, and Jack Brouwer. “Experimental analysis of photovoltaic integration with a proton exchange membrane electrolysis system for power-to-gas”. In: *Int. J. Hydrogen Energy* 42.52 (Dec. 2017), pp. 30569–30583.
- [5] Brahim Laoun, Abdallah Khellaf, Mohamed W Naceur, and Arunachala M Kannan. “Modeling of solar photovoltaic-polymer electrolyte membrane electrolyzer direct coupling for hydrogen generation”. In: *Int. J. Hydrogen Energy* 41.24 (June 2016), pp. 10120–10135.
- [6] Raúl Sarrias-Mena, Luis M Fernández-Ramírez, Carlos Andrés García-Vázquez, and Francisco Jurado. “Electrolyzer models for hydrogen production from wind energy systems”. In: *Int. J. Hydrogen Energy* 40.7 (Feb. 2015), pp. 2927–2938.
- [7] A Saadi, M Becherif, and H S Ramadan. “Hydrogen production horizon using solar energy in Biskra, Algeria”. In: *Int. J. Hydrogen Energy* 41.47 (Dec. 2016), pp. 21899–21912.
- [8] Li Zhao and Jacob Brouwer. “Dynamic operation and feasibility study of a self-sustainable hydrogen fueling station using renewable energy sources”. In: *Int. J. Hydrogen Energy* 40.10 (Mar. 2015), pp. 3822–3837.
- [9] Yildiz Kalinci, Arif Hepbasli, and Ibrahim Dincer. “Techno-economic analysis of a stand-alone hybrid renewable energy system with hydrogen production and storage options”. In: *Int. J. Hydrogen Energy* 40.24 (June 2015), pp. 7652–7664.

- [10] Yoshiaki Shibata. “Economic analysis of hydrogen production from variable renewables”. In: *IEEEJ Energy J* 10.2 (2015), pp. 26–46.
- [11] Byron Hurtubia and Enzo Sauma. “Economic and environmental analysis of hydrogen production when complementing renewable energy generation with grid electricity”. In: *Appl. Energy* 304 (Dec. 2021), p. 117739.
- [12] International Energy Agency. *Global Hydrogen Review*. Tech. rep. IEA, 2023.
- [13] Marcelo Carmo, David L Fritz, Jürgen Mergel, and Detlef Stolten. “A comprehensive review on PEM water electrolysis”. en. In: *Int. J. Hydrogen Energy* 38.12 (Apr. 2013), pp. 4901–4934.
- [14] Omar J Guerra, Joshua Eichman, Jennifer Kurtz, and Bri-Mathias Hodge. “Cost Competitiveness of Electrolytic Hydrogen”. In: *Joule* 3.10 (Oct. 2019), pp. 2425–2443.
- [15] Mariana Corengia and Ana I Torres. “Coupling time varying power sources to production of green-hydrogen: A superstructure based approach for technology selection and optimal design”. In: *Chem. Eng. Res. Des.* 183 (July 2022), pp. 235–249.
- [16] Doo Hyun Chung, Edward J Graham, Benjamin A Paren, Landon Schofield, Yang Shao-Horn, and Dharik S Mallapragada. “Design Space for PEM Electrolysis for Cost-Effective H₂ Production Using Grid Electricity”. In: *Ind. Eng. Chem. Res.* 63.16 (Apr. 2024), pp. 7258–7270.
- [17] Calvin Tsay and Staffan Qvist. “Integrating process and power grid models for optimal design and demand response operation of giga-scale green hydrogen”. en. In: *AIChE J.* 69.12 (Dec. 2023).
- [18] Dharik S Mallapragada, Cristian Junge, Cathy Wang, Hannes Pfeifenberger, Paul L Joskow, and Richard Schmalensee. *Electricity Pricing Problems in Future Renewables-Dominant Power Systems*. CEEPR Working Papers.
- [19] Joannah I Otashu and Michael Baldea. “Demand response-oriented dynamic modeling and operational optimization of membrane-based chlor-alkali plants”. In: *Comput. Chem. Eng.* 121 (Feb. 2019), pp. 396–408.

- [20] Mathias Hofmann, Robert Müller, Andreas Christidis, Peter Fischer, Franziska Klaucke, Sebastian Vomberg, and George Tsatsaronis. “Flexible and economical operation of chlor-alkali process with subsequent polyvinyl chloride production”. en. In: *AIChE J.* 68.1 (Jan. 2022).
- [21] Joris Weigert, Christian Hoffmann, Erik Esche, Peter Fischer, and Jens-Uwe Repke. “Towards demand-side management of the chlor-alkali electrolysis: Dynamic modeling and model validation”. In: *Comput. Chem. Eng.* 149 (June 2021), p. 107287.
- [22] Manuel Espinosa-López, Christophe Darras, Philippe Poggi, Raynal Glises, Philippe Baucour, André Rakotondrainibe, Serge Besse, and Pierre Serre-Combe. “Modelling and experimental validation of a 46 kW PEM high pressure water electrolyzer”. In: *Renewable Energy* 119 (Apr. 2018), pp. 160–173.
- [23] John M Stansberry and Jacob Brouwer. “Experimental dynamic dispatch of a 60 kW proton exchange membrane electrolyzer in power-to-gas application”. In: *Int. J. Hydrogen Energy* 45.16 (Mar. 2020), pp. 9305–9316.
- [24] Mariana Corengia, Nicolás Estefan, and Ana I Torres. “Analyzing Hydrogen Production Capacities to Seize Renewable Energy Surplus”. In: 48 (Jan. 2020). Ed. by Sauro Pierucci, Flavio Manenti, Giulia Luisa Bozzano, and Davide Manca, pp. 1549–1554.
- [25] Marius Holst, Stefan Aschbrenner, Tom Smolinka, Christopher Voglstatter, and Gunter Grimm. *Cost Forecast for Low Temperature Electrolysis - Technology Driven Bottom-Up Prognosis for PEM and Alkaline Water Electrolysis Systems*. Tech. rep. Fraunhofer Institute for Solar Energy Systems, Oct. 2021.
- [26] M Bernt, J Schröter, M Möckl, and H A Gasteiger. “Analysis of Gas Permeation Phenomena in a PEM Water Electrolyzer Operated at High Pressure and High Current Density”. en. In: *J. Electrochem. Soc.* 167.12 (Aug. 2020), p. 124502.
- [27] Christopher Bryce Capuano, Morgan Elizabeth Pertosos, Nemanja Danilovic. “Membrane Electrode Assembly and Method of Making the Same”. 2018/0062192 A1. Mar. 2018.

- [28] Eric Mayousse Nicolas Guillet. “Membrane Electrode Assembly for an Electrolysis Device”. 20140116877 A1. May 2014.
- [29] Alexandra Hartig-Weiß, Maximilian Bernt, Armin Siebel, and Hubert A Gasteiger. “A Platinum Micro-Reference Electrode for Impedance Measurements in a PEM Water Electrolysis Cell”. en. In: *J. Electrochem. Soc.* 168.11 (Nov. 2021), p. 114511.
- [30] Qi Feng, Xiao-zi Yuan, Gaoyang Liu, Bing Wei, Zhen Zhang, Hui Li, and Haijiang Wang. “A review of proton exchange membrane water electrolysis on degradation mechanisms and mitigation strategies”. en. In: *J. Power Sources* 366 (Oct. 2017), pp. 33–55.
- [31] A Weiß, A Siebel, M Bernt, T-H Shen, V Tileli, and H A Gasteiger. “Impact of Intermittent Operation on Lifetime and Performance of a PEM Water Electrolyzer”. en. In: *J. Electrochem. Soc.* 166.8 (Apr. 2019), F487.
- [32] Brian D James, Daniel A DeSantis, Genevieve Saur. *Final Report: Hydrogen Production Pathways Cost Analysis (2013 – 2016)*. Tech. rep. Strategic Analysis Inc, Sept. 2016.
- [33] Michel Suermann, Boris Bensmann, and Richard Hanke-Rauschenbach. “Degradation of proton exchange membrane (PEM) water electrolysis cells: Looking beyond the cell voltage increase”. en. In: *J. Electrochem. Soc.* 166.10 (2019), F645–F652.
- [34] Christoph Rakousky, Uwe Reimer, Klaus Wippermann, Susanne Kuhri, Marcelo Carmo, Wiebke Lueke, and Detlef Stolten. “Polymer electrolyte membrane water electrolysis: Restraining degradation in the presence of fluctuating power”. en. In: *J. Power Sources* 342 (Feb. 2017), pp. 38–47.
- [35] Georgios Papakonstantinou, Gerardo Algara-Siller, Detre Teschner, Tanja Vidaković-Koch, Robert Schlögl, and Kai Sundmacher. “Degradation study of a proton exchange membrane water electrolyzer under dynamic operation conditions”. en. In: *Appl. Energy* 280.115911 (Dec. 2020), p. 115911.

- [36] Shaun M Alia, Sarah Stariha, and Rod L Borup. “Electrolyzer Durability at Low Catalyst Loading and with Dynamic Operation”. en. In: *J. Electrochem. Soc.* 166.15 (Oct. 2019), F1164.
- [37] Na Li, Samuel Simon Araya, and Søren Knudsen Kær. “Investigating low and high load cycling tests as accelerated stress tests for proton exchange membrane water electrolysis”. In: *Electrochim. Acta* 370 (Feb. 2021), p. 137748.
- [38] Shucheng Sun, Zhigang Shao, Hongmei Yu, Guangfu Li, and Baolian Yi. “Investigations on degradation of the long-term proton exchange membrane water electrolysis stack”. In: *J. Power Sources* 267 (Dec. 2014), pp. 515–520.
- [39] Steffen Henrik Frensch, Frédéric Fouda-Onana, Guillaume Serre, Dominique Thoby, Samuel Simon Araya, and Søren Knudsen Kær. “Influence of the operation mode on PEM water electrolysis degradation”. In: *Int. J. Hydrogen Energy* 44.57 (Nov. 2019), pp. 29889–29898.
- [40] Julio José Caparrós Mancera, Francisca Segura Manzano, José Manuel Andújar, Francisco José Vivas, and Antonio José Calderón. “An Optimized Balance of Plant for a Medium-Size PEM Electrolyzer: Design, Control and Physical Implementation”. en. In: *Electronics* 9.5 (May 2020), p. 871.
- [41] Kosan Roh, Luisa C Brée, Karen Perrey, Andreas Bulan, and Alexander Mitsos. “Flexible operation of switchable chlor-alkali electrolysis for demand side management”. In: *Appl. Energy* 255 (Dec. 2019), p. 113880.
- [42] Mohd Adnan Kahn, Cameron Young, Catherine Mackinnon, and David B Layzell. *The Techno-Economics of Hydrogen Compression*. Tech. rep. The Transition Accelerator, Oct. 2021.
- [43] Thaneer Malai Narayanan, Guannan He, Emre Gençer, Yang Shao-Horn, and Dharik S Mallapragada. “Role of Liquid Hydrogen Carriers in Deeply Decarbonized Energy Systems”. In: *ACS Sustainable Chem. Eng.* 10.33 (Aug. 2022), pp. 10768–10780.

- [44] Leander Kotzur, Peter Markewitz, Martin Robinius, and Detlef Stolten. “Time series aggregation for energy system design: Modeling seasonal storage”. en. In: *Appl. Energy* 213 (Mar. 2018), pp. 123–135.
- [45] G Sandhya Rani, Sarada Jayan, and K V Nagaraja. “An extension of golden section algorithm for n-variable functions with MATLAB code”. In: *IOP Conf. Ser. Mater. Sci. Eng.* 577.1 (Nov. 2019), p. 012175.
- [46] Bethany Nicholson, John D Sirola, Jean-Paul Watson, Victor M Zavala, and Lorenz T Biegler. “pyomo.dae: a modeling and automatic discretization framework for optimization with differential and algebraic equations”. In: *Math. Program. Comput.* (2018).
- [47] Andreas Wächter and Lorenz T Biegler. “On the implementation of an interior-point filter line-search algorithm for large-scale nonlinear programming”. en. In: *Math. Program.* 106.1 (Mar. 2006), pp. 25–57.
- [48] *HSL, a collection of Fortran codes for large-scale scientific computation. See <https://www.hsl.rl.ac.uk>.*
- [49] A Reuther, J Kepner, C Byun, S Samsi, W Arcand, David Bestor, Bill Bergeron, V Gadepally, Michael Houle, M Hubbell, Michael Jones, Anna Klein, Lauren Milechin, J Mullen, Andrew Prout, Antonio Rosa, Charles Yee, and P Michaleas. “Interactive supercomputing on 40,000 cores for machine learning and data analysis”. In: *HPEC* (July 2018), pp. 1–6.
- [50] Jason K Lee, Chunghyuk Lee, Kieran F Fahy, Benzhong Zhao, Jacob M LaManna, Elias Baltic, David L Jacobson, Daniel S Hussey, and Aimy Bazylak. “Critical Current Density as a Performance Indicator for Gas-Evolving Electrochemical Devices”. In: *Cell Reports Physical Science* 1.8 (Aug. 2020), p. 100147.
- [51] F Marangio, M Pagani, M Santarelli, and M Cali. “Concept of a high pressure PEM electrolyser prototype”. In: *Int. J. Hydrogen Energy* 36.13 (July 2011), pp. 7807–7815.
- [52] Agate Martin, Patrick Trinke, Boris Bensmann, and Richard Hanke-Rauschenbach. “Hydrogen Crossover in PEM Water Electrolysis at Current Densities up to 10 A cm⁻²”. en. In: *J. Electrochem. Soc.* 169.9 (Sept. 2022), p. 094507.

- [53] *ERCOT Market Prices*. en. <https://www.ercot.com/mktinfo/prices>. Accessed: 2023-11-16.
- [54] Pieter Gagnon, Brady Cowiestoll, and Marty Schwarz. *Cambium 2022 Scenario Descriptions and Documentation*.
- [55] Guannan He, Dharik S Mallapragada, Abhishek Bose, Clara F Heuberger-Austin, and Emre Gençer. “Sector coupling via hydrogen to lower the cost of energy system decarbonization”. en. In: *Energy Environ. Sci.* 14.9 (Sept. 2021), pp. 4635–4646.
- [56] Christine Minke, Michel Suermann, Boris Bensmann, and Richard Hanke-Rauschenbach. “Is iridium demand a potential bottleneck in the realization of large-scale PEM water electrolysis?” In: *Int. J. Hydrogen Energy* 46.46 (July 2021), pp. 23581–23590.
- [57] Rebecca Riedmayer, Benjamin A Paren, Landon Schofield, Yang Shao-Horn, and Dharik Mallapragada. “Proton exchange membrane electrolysis performance targets for achieving 2050 expansion goals constrained by iridium supply”. en. In: *Energy Fuels* 37.12 (June 2023), pp. 8614–8623.
- [58] Maximilian Bernt, Armin Siebel, and Hubert A Gasteiger. “Analysis of Voltage Losses in PEM Water Electrolyzers with Low Platinum Group Metal Loadings”. en. In: *J. Electrochem. Soc.* 165.5 (Mar. 2018), F305.

Table S1: Set Nomenclature

Name	Description	Units	Value	Notes
Set Indices				
$i \in I$	Chemical species	-	$\{\text{H}_2, \text{O}_2, \text{H}_2\text{O}, \text{N}_2\}$	-
$j \in J$	Stream numbers	-	$\{1, 2, \dots, 16\}$	-
$k \in K$	Anode/Cathode	-	$\{\text{an}, \text{cat}\}$	-
$r \in D_r$	Representative days	-	$\{1, 2, \dots, 7\}$	-
$d \in D$	Actual days	-	$\{1, 2, \dots, 365\}$	-

5 Supporting Information

5.1 Mass and Energy Balance and Electrochemical Relations

The following is a detailed description of the mass and energy balances as well as the electrochemical relations used in this work. Tables S1 - S3 outline the nomenclature used in this work.

5.1.1 PEM Electrolyzer Potentials

The current and voltage relationship used in this work borrows from the work done by [3, 6, 8] and follows a standard procedure of estimating open circuit voltage and related overpotentials for the system as seen in Equation S1. The total voltage is then the sum of these potentials.

$$V_{total} = V_{oc} + V_{act} + V_{ohm} + V_{deg} \quad (\text{S1})$$

Degradation of the cell appears as an increase in operating voltage of the cell. Discussion of the calculation of degradation for a cell as a function of usage is presented in the Optimization section.

Thermodynamic Potential Thermodynamic voltage is described by the free energy of reaction as shown in Equation S2. In general, this free energy of reaction as well as the entropy and enthalpy are functions of pressure and temperature.

$$V_{rev} = \frac{\Delta G}{2F} \quad (\text{S2})$$

$$\Delta G = \Delta H - T\Delta S \quad (\text{S3})$$

For this work, the enthalpy and entropy are assumed to be functions of temperature only. Correlations used to estimate enthalpies and entropies for H_2O , H_2 , and O_2 were taken from the NIST webbook [5].

Table S2: Parameter Nomenclature

Name	Description	Units	Value	Notes
F	Faraday's constant	$\frac{\text{C}}{\text{mol}}$	96,485	-
A_{cell}	Catalytic active area	cm^2	450	[1]
A_{mem}	Area of membrane/Size of one cell	cm^2	450	[1]
δ_{el}	Thickness of electrode	cm	8.0×10^{-3}	[2]
v_{an}	Anode volume	mL	$\approx \delta_{el} A_{mem}$	-
v_{cat}	Cathode volume	mL	$\approx \delta_{el} A_{mem}$	-
δ_{mem}	Membrane thickness	cm	1.75×10^{-2}	[3]
n_g	Electro-osmotic drift coefficient	unitless	-	[4], Equation S17
ΔG°	Standard free energy of reaction	$\frac{\text{kJ}}{\text{mol}}$	237.2	[3]
R_{gas}	Gas constant	$\frac{\text{J}}{\text{mol K}}$	8.314	-
T_{ref}	Reference temperature for thermo	K	298	[3]
H_i	Enthalpy of species i	$\frac{\text{J}}{\text{mol}}$	-	[5]
$C_{p,th}$	Lumped thermal capacitance	$\frac{\text{J}}{\text{K}}$	-	Scaled from [6]
R_{th}	Thermal resistance of stack	$\frac{\text{s}}{\text{JK}}$	-	Scaled from [6]
$i_{0,an,ref}$	Exchange current density at T_{ref}	$\frac{\text{A}}{\text{cm}^2}$	5×10^{-12}	[3]
$i_{0,cat,ref}$	Exchange current density at T_{ref}	$\frac{\text{A}}{\text{cm}^2}$	1×10^{-3}	[3]
α_{an}	Bulter-Volmer equation parameter	-	-	Fitted parameter
α_{cat}	Bulter-Volmer equation parameter	-	-	Fitted parameter
$\gamma_{M,an}$	Anode roughness factor	-	1198	Equation S8
$\gamma_{M,cat}$	Cathode roughness factor	-	286	Equation S8
φ_I	Fraction of metal catalyst in contact with ionomer	-	0.75	[3]
$m_{M,an}$	Catalyst loading at anode	$\frac{\text{g}}{\text{cm}^2}$	0.9×10^{-3}	[7]
$m_{M,cat}$	Catalyst loading at cathode	$\frac{\text{g}}{\text{cm}^2}$	0.3×10^{-3}	[7]
$\rho_{M,an}$	Catalyst density anode	$\frac{\text{g}}{\text{cm}^3}$	11.66	[7]
$\rho_{M,cat}$	Catalyst density cathode	$\frac{\text{g}}{\text{cm}^3}$	21.45	[7]
$d_{M,an}$	Catalyst crystal diameter anode	cm	2.9×10^{-7}	[7]
$d_{M,cat}$	Catalyst crystal diameter cathode	cm	2.2×10^{-7}	[7]
λ_m	Hydration factor of PEM	$\frac{\text{mol}_{\text{H}_2\text{O}}}{\text{mol}_{\text{SO}_3}}$	21	[8], Equation S11
σ_{mem}	Conductance of membrane	-	-	[8], Equation S12
p_{elec}	Price of electricity	-	-	[9, 10]
p_{water}	Price of water	$\frac{\$}{1000 \text{ gal}}$	2.78	[11]

Table S3: Variable Nomenclature

Name	Description	Units	Value	Primary Decision Variable	Notes
$i(t)$	Current density	$\frac{A}{cm^2}$	0.1 – 4	✓	-
$\dot{n}_{H_2O,1}(t)$	Inlet water flowrate	$\frac{mol}{s}$	0 – 50,000	✓	base case
$\dot{n}_3(t)$	Total flow out of anode	$\frac{mol}{s}$	0 – $10N_c \frac{A_{cat} i}{4F}$	✓	base case
$\dot{n}_4(t)$	Total flow out of cathode	$\frac{mol}{s}$	0 – $10N_c \frac{A_{cat} i}{2F}$	✓	base case
$\dot{n}_{13}(t), \dot{n}_{14}$	Split between satisfying demand and storage	$\frac{mol}{s}$	0 – 10^6	✓	base case
$\dot{n}_{16}(t)$	Flowrate out of storage	$\frac{mol}{s}$	0 – 10^6	✓	base case
$\dot{n}_{11}(t)$	Flowrate of N ₂	$\frac{mol}{s}$	0 – 10^3	✓	base case
$N_i(t)$	Moles of species i	mol	-		-
$\dot{n}_{i,j}(t)$	Molar flow rate of species j in stream i	$\frac{mol}{s}$	-		-
$y_{j,k}(t)$	Mole fraction of species j in stream at electrode k	-	-		-
$T(t)$	Temperature of anode and cathode	°C	60 – 80 60 – 90		base case sensitivity
X_{H_2}	Conversion of hydrogen crossing from cathode to anode	-	0.9		base case
$V^{total}(t)$	Cell voltage	V	-		base case
$V_d^{undeg}(t)$	Cell voltage not including degradation on day d	V	-		base case
$\delta V_r^{deg}(t)$	Intra-day change in degradation up to time t	V	-		base case
$V_d^{cuml,deg}(t)$	Cumulative degradation up to day d and time t	V	-		base case
C^{elec}	Annual cost of electricity	\$	-		base case
$C^{BoP,elec}$	Annual cost of electricity used by balance of plant	\$	-		base case
C^{water}	Annual cost of de-ionized water	\$	-		base case
C^{N_2}	Annual cost of purge nitrogen	\$	-		base case
δ_r	Change in storage over representative period r	mol	-		
Λ_{H_2}	Hydrogen storage	mol	-		

The Nernst Equation corrects this thermodynamic voltage for conditions other than the standard condition.

$$V_{oc} = V_{rev} - \frac{RT}{2F} \ln \left(\frac{a_{H_2O}}{a_{H_2} a_{O_2}^{1/2}} \right) \quad (S4)$$

$$V_{oc} = V_{rev} + \frac{RT}{2F} \ln \left(\frac{P_{H_2}}{P^\circ} \sqrt{\frac{P_{O_2}}{P^\circ}} \right) \quad (S5)$$

As is consistent with other PEM electrolyzers models, the activity of water is assumed to be unity in order to reduce Equation S4 to Equation S5 [3, 6, 8]. The reference pressure is assumed to be 1 bar with P_{H_2} and P_{O_2} being 30 bar and 1 bar, respectively.

Activation Overpotential Activation overpotential is determined using the Butler-Volmer equation applied to the anode and cathode. The sum of the resulting overpotentials is the total activation overpotential.

$$V_{act} = \frac{RT}{\alpha_{an} F} \operatorname{arcsinh} \left(\frac{i}{2i_{0,an}} \right) + \frac{RT}{\alpha_{cat} F} \operatorname{arcsinh} \left(\frac{i}{2i_{0,cat}} \right) \quad (S6)$$

According to the kinetic theory used to derive the Butler-Volmer equation above, α_{an} and α_{cat} should sum to the number of electrons transferred in the reaction [12]. As such, for

a PEM, system they should sum to 2. However, in literature, α_{an} , α_{cat} , $i_{0,an}$, and $i_{0,cat}$ are used as fitting parameters for models when data for a polarization curve is available. This had led to a wide variety of charge transfer coefficients and exchange current densities. For this model charge transfer coefficients were left as fitting parameters for the system with the constraint that their sum could not exceed $n = 2$. Parameters were found as minimization of the sum of squared errors. Reference exchange current densities were chosen from typical values used in literature and corrected for temperature and roughness of the catalyst by Equations S7 - S9 as was done by Görgün et al [8, 13].

$$i_{0,k}^* = i_{0,ref,k} e^{\left[\frac{-E_a}{R} \left(\frac{1}{T} - \frac{1}{T_{ref}} \right) \right]} \quad (S7)$$

$$\gamma_{M,k} = \varphi_l m_{M,k} \frac{6}{\rho_{M,k} d_{M,k}} \quad (S8)$$

$$i_{0,k} = \gamma_{M,k} i_{0,k}^* \quad (S9)$$

Ohmic Overpotential The ohmic resistance is a function of the thickness of the membrane, membrane conductivity, and operating current density. Membrane conductivity is a function of membrane hydration and operating temperature of the electrolyzer as seen in Equations S10 - S12. Görgün et al used an empirical relation for the water hydration factor, λ_m , and σ_{mem} where $\frac{1}{\sigma_{mem}} = R_{ohm}$ [8]. Under normal operating conditions the activity of water is such that $\lambda_m \approx 21$, which was the value used for this study [14].

$$V_{ohm} = \frac{\delta_{mem}}{\sigma_{mem}} i \quad (S10)$$

$$\lambda_m = 0.43 + 17.81 a_{H_2O} - 39.85 a_{H_2O}^2 + 36 a_{H_2O}^3 \quad (S11)$$

$$\sigma_{mem} = (0.00514 \lambda_m - 0.00326) e^{(1268 \left(\frac{1}{303} - \frac{1}{T} \right))} \quad (S12)$$

5.1.2 PEM Electrolyzer Mass Balances

Anode

A transient water balance around the electrolyzer is shown in Equation S13.

$$\frac{dN_{H_2O,an}}{dt} = \dot{n}_{H_2O,2} - \dot{n}_{H_2O,3} - \dot{n}_{H_2O,3}^{vap} - \dot{n}_{H_2O,cross} - \dot{n}_{H_2O,consum} + \dot{n}_{H_2O,gen} \quad (S13)$$

$$0 = \dot{n}_{H_2O,2} - \dot{n}_{H_2O,3} - \dot{n}_{H_2O,3}^{vap} - \dot{n}_{H_2O,cross} - \dot{n}_{H_2O,consum} + \dot{n}_{H_2,cross} X_{H_2} \quad (S14)$$

As is done on the industrial scale, the system is fed with excess water. As such, flows of water in and out of the anode are much greater than any liquid and vapor holdup in the

anode. Therefore to simplify the system, the derivative term is assumed to be approximately zero in Equation S14. It is also assumed there is a recombination catalyst embedded in the anode side of the membrane which has a 90% conversion of H_2 and O_2 to H_2O . Conversion of hydrogen is represented by X_{H_2} . This recombination catalyst is a standard part of industrially operating PEM electrolyzers and are used to reduce the chance of a safety event occurring at the anode [15, 16].

$\dot{n}_{H_2O,2}$ represents the liquid flowrate of water into the anode, and $\dot{n}_{H_2O,3}$ represents the liquid flowrate of water out of the anode. Other terms in the steady state water balance in Equation S14, are defined below:

$$\dot{n}_{H_2O,3}^{vap} = \frac{P_{H_2O}^{sat}}{P_{an}} \dot{n}_{gas,3} \quad (S15)$$

$$\dot{n}_{H_2O,cross} = N_c \frac{n_g i A}{2F} \quad (S16)$$

$$n_g = 2.27 - 0.70i - 0.02P + 0.02Pi + 0.003T + 0.005iT - 0.0002PT \quad (S17)$$

$$\dot{n}_{H_2O,gen} = N_c \frac{iA}{2F} \quad (S18)$$

In Equation S15, water vapor is assumed to be in equilibrium with liquid water at the temperature of the cell in accordance with Raoult's Law. Equations S16 and S17 combined describe the electro-osmotic drift of water from anode to cathode at a given temperature, cathode pressure, and operating current density as described by Medina et al. [4]. Equation S18 describes the consumption of water by Faraday's law assuming 100% faradaic efficiency.

Balances for oxygen and hydrogen at the anode are shown below in Equations S19-S22. Each species is based on a mole balance with Faraday's law of electrolysis modeling the electrochemical reaction term.

$$\frac{dN_{O_2,an}}{dt} = \dot{n}_{O_2,gen} - \dot{n}_{O_2,3} - \frac{1}{2} \dot{n}_{H_2,cross} X_{H_2} \quad (S19)$$

$$= N_c \frac{iA_{cell}}{4F} - y_{O_2,an} \dot{n}_{gas,3} - \frac{1}{2} \dot{n}_{H_2,cross} X_{H_2} \quad (S20)$$

$$\frac{dN_{H_2,an}}{dt} = \dot{n}_{H_2,cross}(1 - X_{H_2}) - \dot{n}_{H_2,out} \quad (S21)$$

$$= 0.31 \frac{iA_{cell}}{2F} (P_{H_2,cat} - P_{H_2,an})(1 - X_{H_2}) - y_{H_2,an} \dot{n}_{gas,3} \quad (S22)$$

Equation S19 represents the transient mole balance on oxygen. It is assumed the oxygen concentration of the water entering the anode is near zero, hence there is no oxygen flow into the anode. Equation S20 is the same transient mole balance rearranged assuming oxygen is an ideal gas.

Equation S21 represents the transient mole balance on hydrogen. The only way hydrogen can enter the anode is through crossover from the cathode, and the only way hydrogen can

exit is through the anode exit gas stream. Equation S22 is the same transient mole balance rearranged assuming hydrogen as an ideal gas and using the hydrogen crossover correlation investigated by Bernt et. al [17].

Cathode

A transient water balance on the cathode with the same holdup assumptions as the anode is shown in Equations S23 - S24

$$\frac{dN_{H_2O,cat}}{dt} = \dot{n}_{H_2O,cross} - \dot{n}_{H_2O,4} - \dot{n}_{H_2O,4}^{vap} \quad (S23)$$

$$0 = \dot{n}_{H_2O,cross} - \dot{n}_{H_2O,4} - \dot{n}_{H_2O,4}^{vap} \quad (S24)$$

The material balance for hydrogen and at the cathode are shown below in Equations S25 - S26. Each species is based on a mole balance with Faraday's law of electrolysis modeling the electrochemical reaction term and gases are assumed ideal.

$$\frac{dN_{H_2}}{dt} = \dot{n}_{H_2,gen} - \dot{n}_{H_2,4} - \dot{n}_{H_2,cross} \quad (S25)$$

$$\frac{dN_{H_2}}{dt} = N_c \frac{iA}{2F} - y_{H_2} \dot{n}_{gas,4} - 0.31 \frac{iA_{cell}}{2F} (P_{H_2,cat} - P_{H_2,an})(1 - X_{H_2}) \quad (S26)$$

Oxygen crossover is assumed negligible as the oxygen is much less permeable to the Nafion membrane, and the cathode is pressurized meaning oxygen transport will be effectively zero [17].

5.1.3 PEM Electrolyzer Energy Balance

The energy balance is based on a lumped capacitance model described in Equations S27-S31. Water enters the anode at ambient conditions so that $T_{in} = T_{ref}$. Espinosa-Lopez et. al presented a thermal lumped capacitance model for a 60 cell PEM electrolyzer stack in which they reported a lumped thermal capacitance $C_{p,th}$ and thermal resistance R_{th} normalized by the area of the cell [6]. These values for the lumped thermal capacitance and heat loss resistance were used in the model as a reference and scaled up or down based on the area of the modeled system. V_{th} is the thermoneutral voltage of the cell, assumed to be 1.48 V.

$$\frac{dT}{dt} = \frac{1}{C_{p,th}} \left(\dot{H}_{in} - \dot{H}_{out} + \dot{Q}_{gen} - \dot{Q}_{loss} \right) \quad (\text{S27})$$

$$\dot{W}_{in} = \sum_i n_{i,in} H_i(T_{in}) \quad (\text{S28})$$

$$\dot{W}_{out} = \sum_i n_{i,out} H_i(T_{cell}) \quad (\text{S29})$$

$$\dot{Q}_{gen} = N_c (V_{total} - V_{tn}) iA \quad (\text{S30})$$

$$\dot{Q}_{loss} = \frac{1}{R_{th}} (T - T_{ambient}) \quad (\text{S31})$$

$$(\text{S32})$$

The standard enthalpies of formation are included in the thermoneutral voltage, and $T_{ref} = T_{in} = T_{ambient}$ for the thermodynamic calculations. This is consistent with the energy balance presented in Espinosa et al and allows the heat generation term to be written as the potential applied over the thermoneutral voltage [6].

Equation S27 represents the overall energy balance for the system including all possible sources and sinks for heat. Equations S28 - S31 define those sinks and sources. For the energy in, species include water and nitrogen (if used), and for the energy out species include, water, water vapor, nitrogen (if used), hydrogen, and oxygen.

5.2 K-Means Clustering for Representative Days

K-means clustering was performed on the input price data series of hourly electricity prices. The k-means clustering algorithm works to find k centroids to which each of the 365 days in the year most closely correspond.

Once each day is assigned a cluster, the day closest to the cluster centroid is chosen as the representative day for that cluster. Each of these representative days then have an associated weight which signifies the number of real days that belong to the cluster. This way, the optimization can be performed in a significantly reduced time domain while still capturing much of the variability in electricity price seen throughout the year.

5.3 Storage Formulation

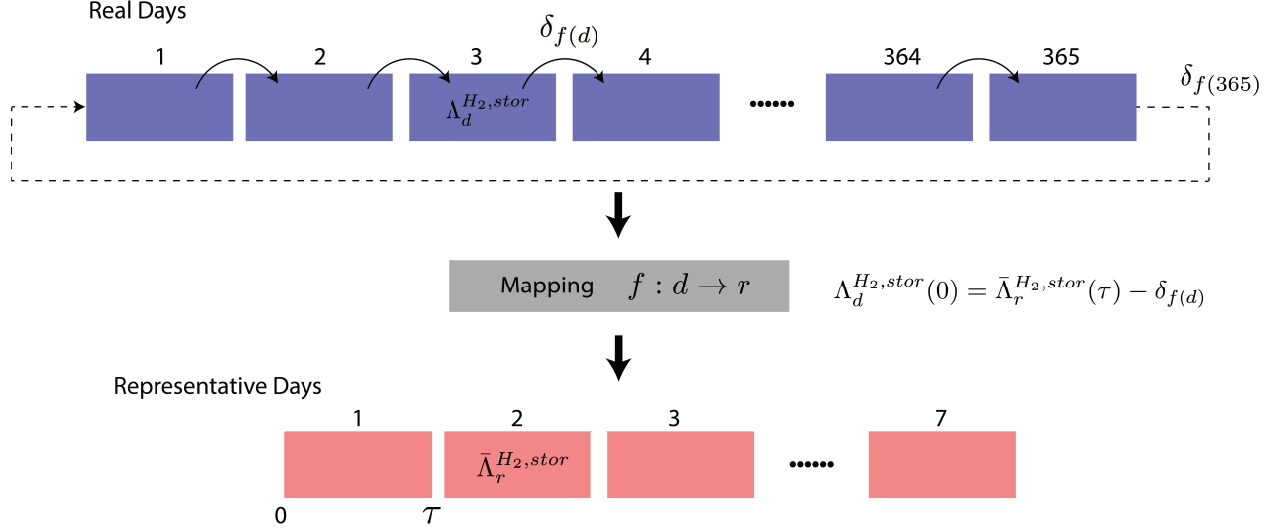


Figure S1: Storage formulation and connection between representative days and real days. Each real day has an hour to hour changing amount of storage $\Lambda_d^{H_2,stor}$. Each real day is mapped to a representative day by the k-means clustering mapping $f : d \rightarrow r$. Thus each representative day has an hour to hour changing amount of storage $\bar{\Lambda}_r^{H_2,stor}$. δ_r allows for carry over of storage between real days. To relate the representative days to real days, the beginning of a real day of storage must match the end of the corresponding representative day minus the carry over associated with the representative day which is summarized in the equation in this figure.

5.4 Convergence Time

Table S4: Convergence time for scenarios presented in the paper. Each case took 15 iterations of the GSS in order to converge within 0.1% tolerance.

Case	Time (hours)
Degradation 2022 Base Case	44.8
No Degradation	25.2
Degradation, West Texas	74.3
Degradation, Fixed CAPEX	–
High Temperature	57.6
No Safety Constraint, Fixed CAPEX	–
Degradation 2030 Base Case	52.1
2030 High CAPEX	48.4
2030 Low CAPEX	43.7
2030 High Decarbonization	45.7
2030 Low Decarbonization	49.4

5.5 Algorithm Scaling

Convergence time increases with an increasing number of representative days. The vast majority of constraints for each problem type are equality constraints. The LCOH seems to be converging to a singular value, albeit non monotonically. Theoretically, as the number of representative days approaches the number of real days, the LCOH would approach the real LCOH which is the LCOH of using the full price series data. 7 representative days was chosen for this study for the base case's ability to converge < 48 hours. For this particular price series it happens to be the number of representative days that has the lowest LCOH, though it was not chosen for that reason.

Table S5: Convergence time for different numbers of representative days. Each case was run with the base case South LZ price series with degradation.

Representative Days	LCOH (\$/kg)	Convergence Time (hours)	Number of Variables	Number of Equality Constraints	Number of Inequality Constraints	Number of GSS Iterations	Avg. GSS Iteration Time (min)
2	\$ 6.96	23.3	188,469	186,728	776	15	21.8
4	\$ 6.92	31.5	199,913	196,796	1,552	15	29.5
7	\$ 6.60	44.8	217,079	211,898	2,716	15	39.6
9	\$ 6.83	49.4	228,523	221,966	3,492	15	46.3
10	\$ 7.06	57.5	234,245	227,000	3,880	15	53.9
14	\$ 7.19	82.3	257,133	247,136	5,432	15	77.2

5.6 Results from Alternate Scenarios

5.6.1 Degradation Sensitivities

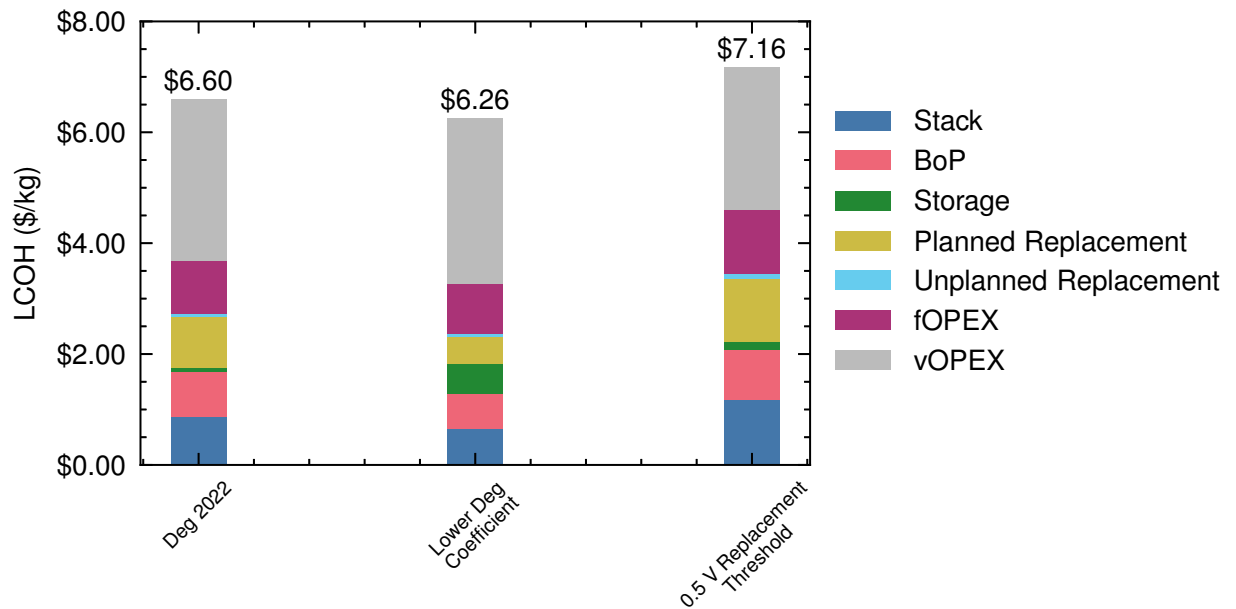


Figure S2: Sensitivity to the degradation correlation coefficient being reduced to 15 (middle bar) and the replacement threshold voltage being reduced to 0.5 V (right bar) are compared against the base degradation case (left bar). Somewhat unsurprisingly a less aggressive degradation rate results in a lower levelized cost. Reducing the maximum amount of degradation that can occur before stack replacement increases LCOH.

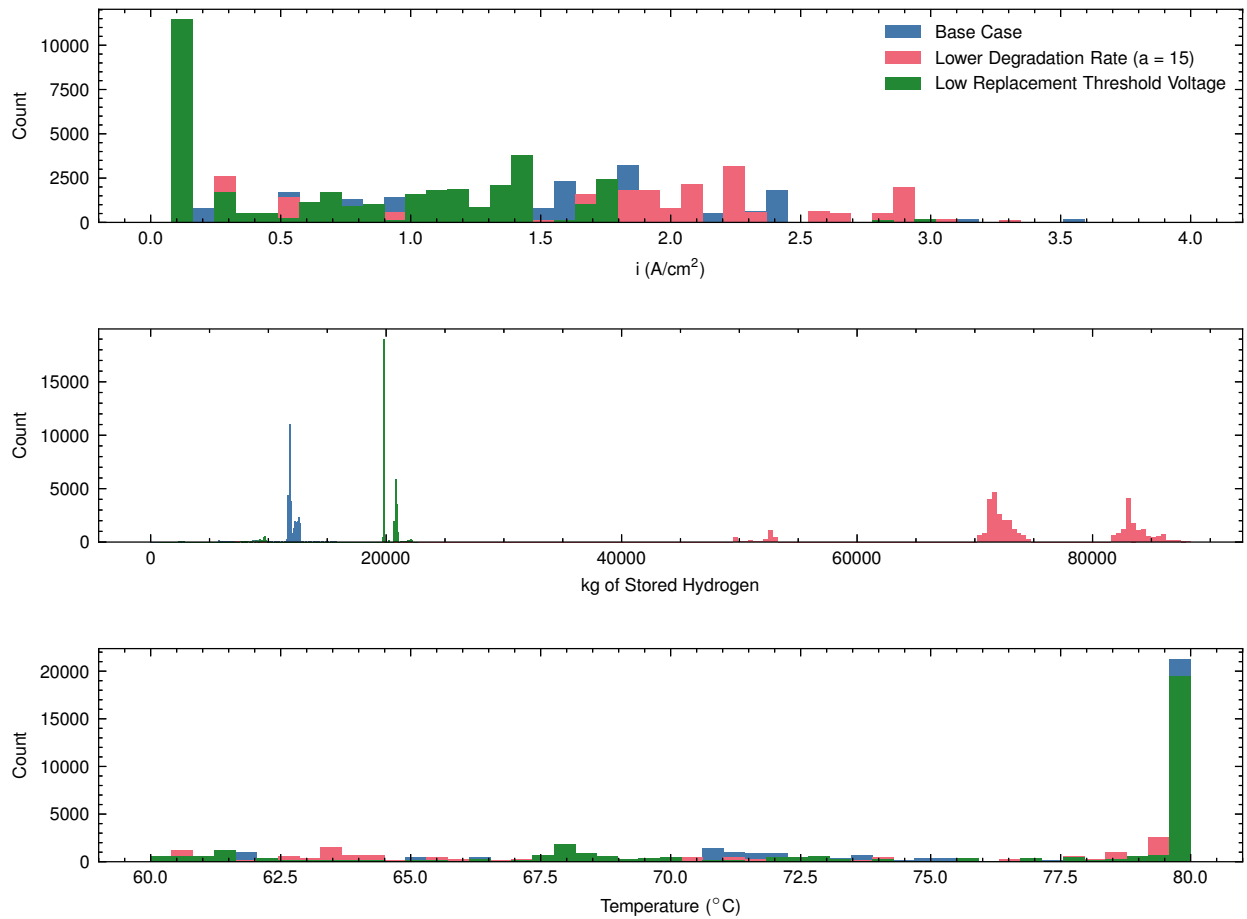


Figure S3: Changing the underlying assumptions on degradation shifts the operating profile from the base case. With less degradation occurring when $a = 15$, the model is free to operate at higher current densities than the base case. Additionally when the replacement threshold voltage is lowered the model is incentivized to keep replacement rates as high as possible by degrading as little as possible.

5.6.2 Degradation with CAPEX Fixed at No Degradation Result

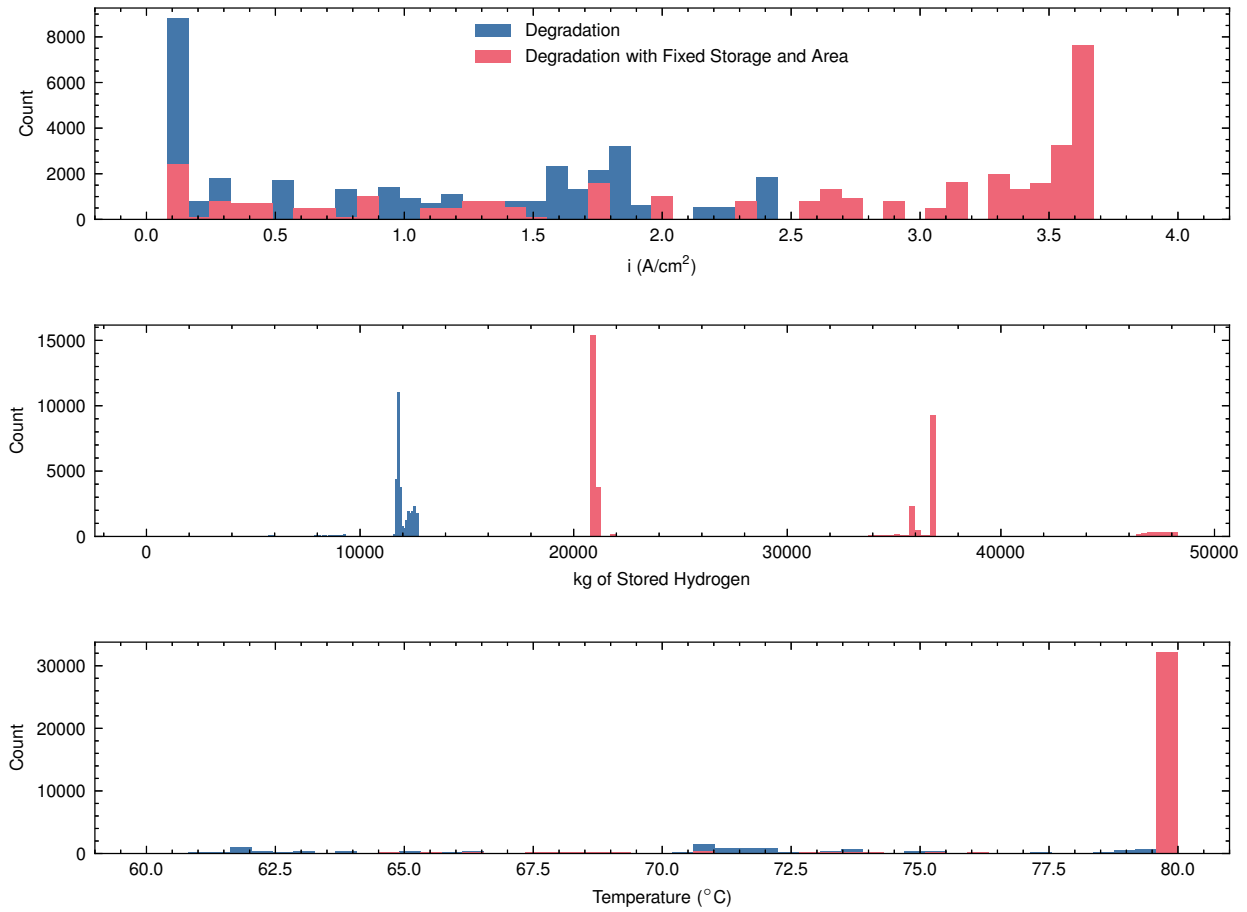


Figure S4: Current density, storage, and temperature distributions for the base degradation case and the degradation case run with the stack size and storage size of the no degradation case. Fixing the stack size and storage results in having to operate at much higher current densities and more frequent replacements.

5.6.3 Impact of Higher Temperature

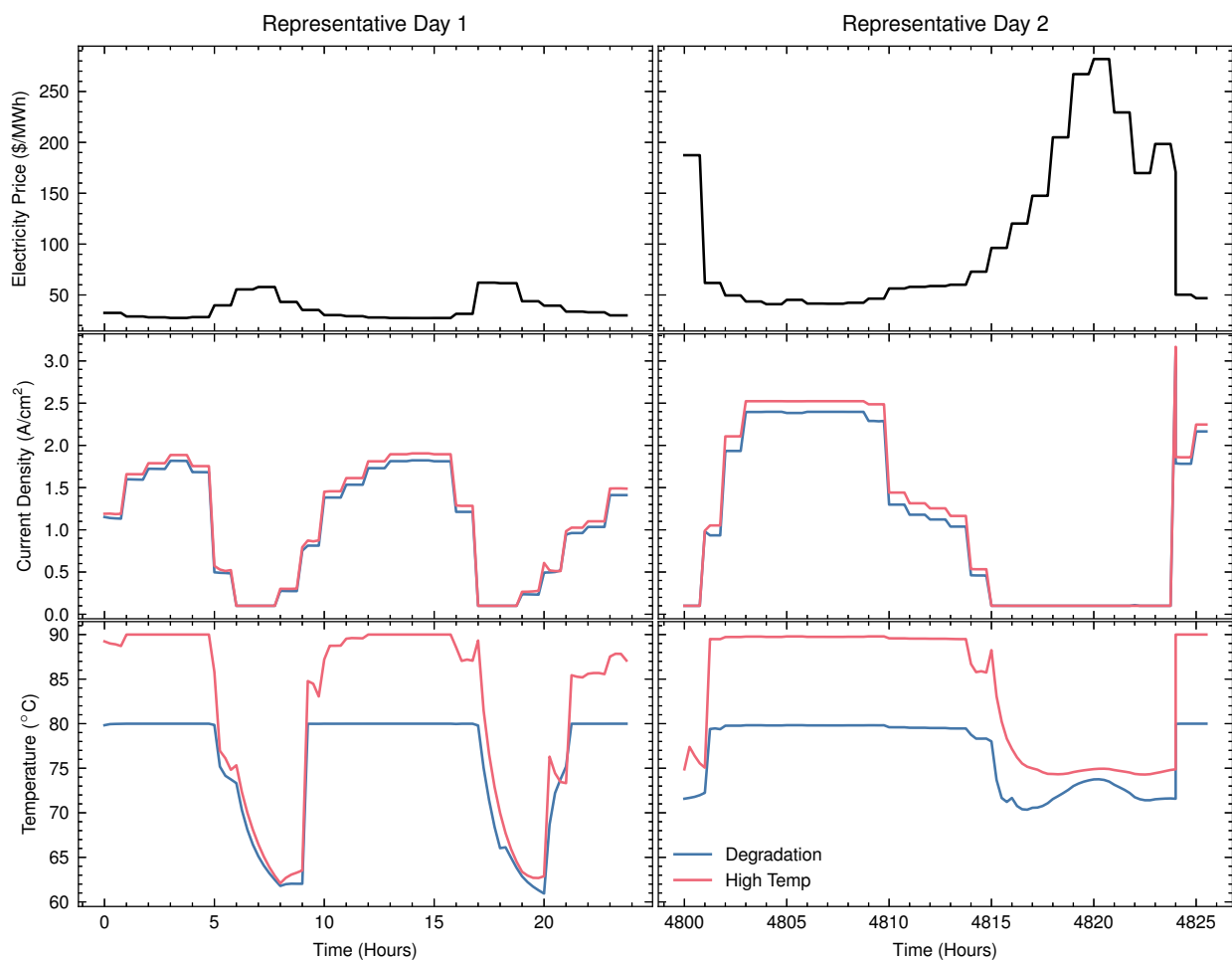


Figure S5: Current density profile and temperature profile of scenario where the upper bound of the temperature limit is changed from 80°C to 90°C. Current density operation is nearly the same for both cases with the case with a higher temperature upper bound operating at slightly higher current densities. This coincides with a larger amount of storage sized for this system.

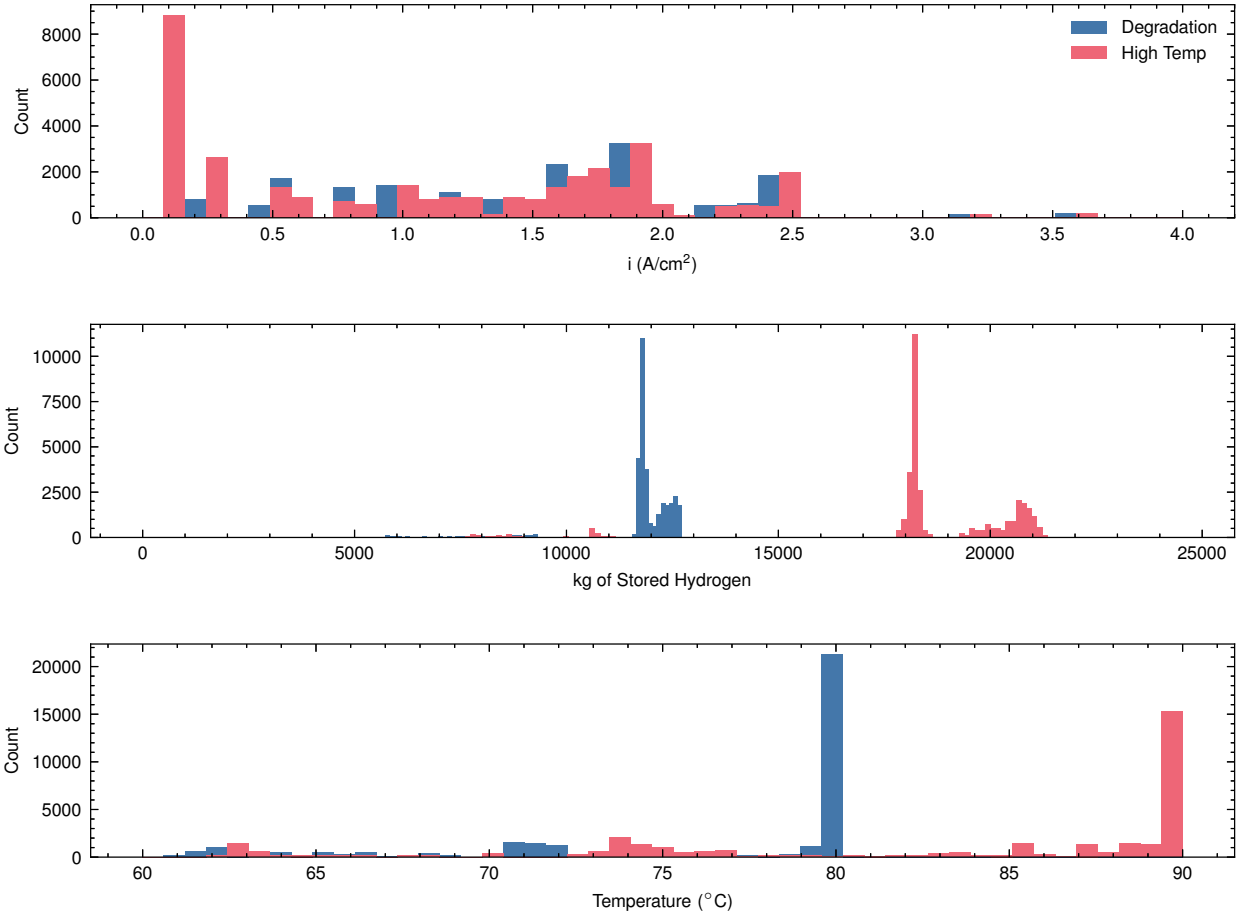


Figure S6: Higher temperature upper bound case current density, storage, and temperature distribution. The high temperature case operates at slightly higher current densities overall and as a result sizes and utilizes a greater amount of storage than the base degradation case.

5.6.4 Impact of Recombination Catalyst and Safety Constraint

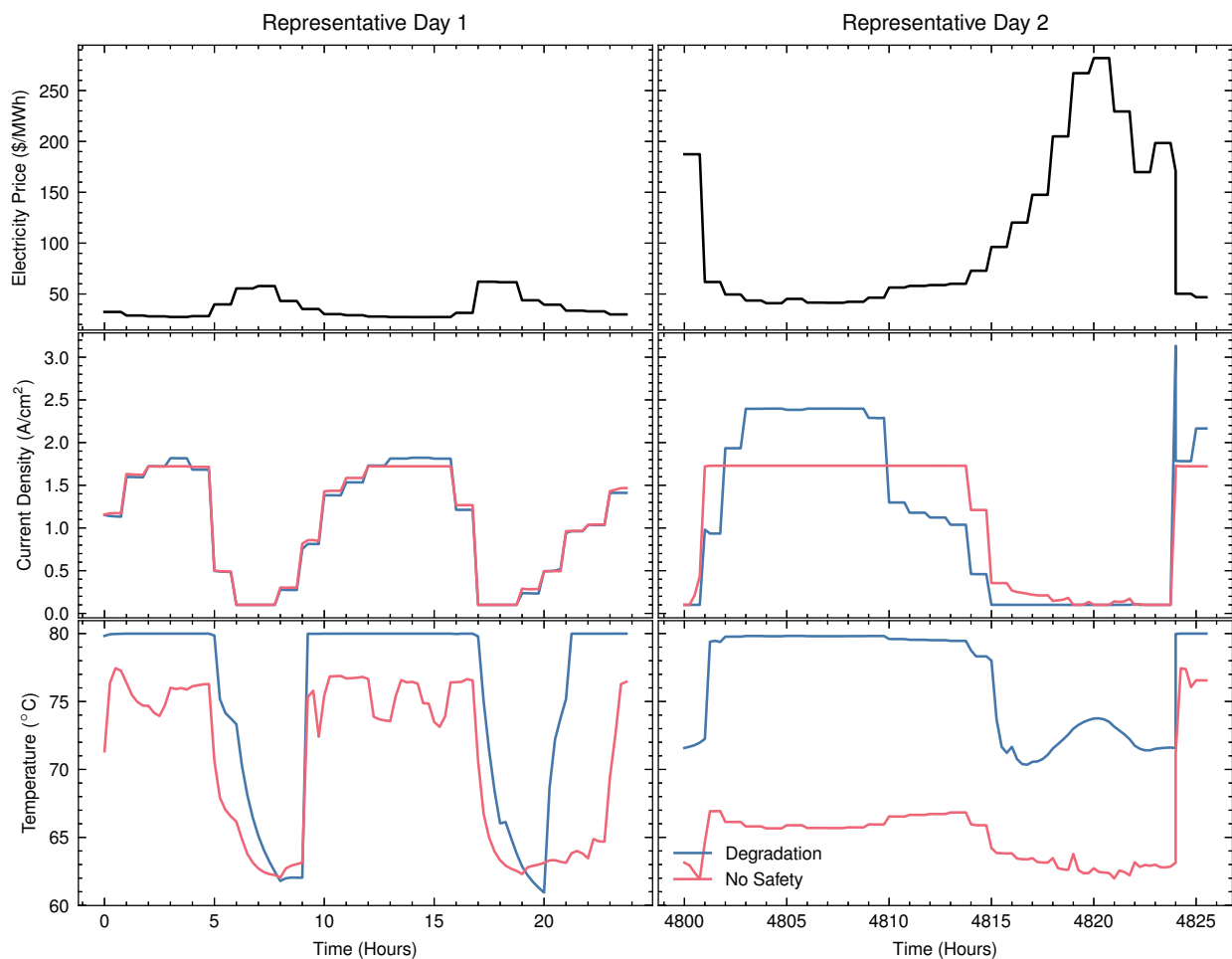


Figure S7: Operational profiles for the case with no safety constraint. The case without a safety constraint operates at lower current densities since it does not have to maintain O₂ production at the anode to keep the H₂ concentration below the lower flammability limit.

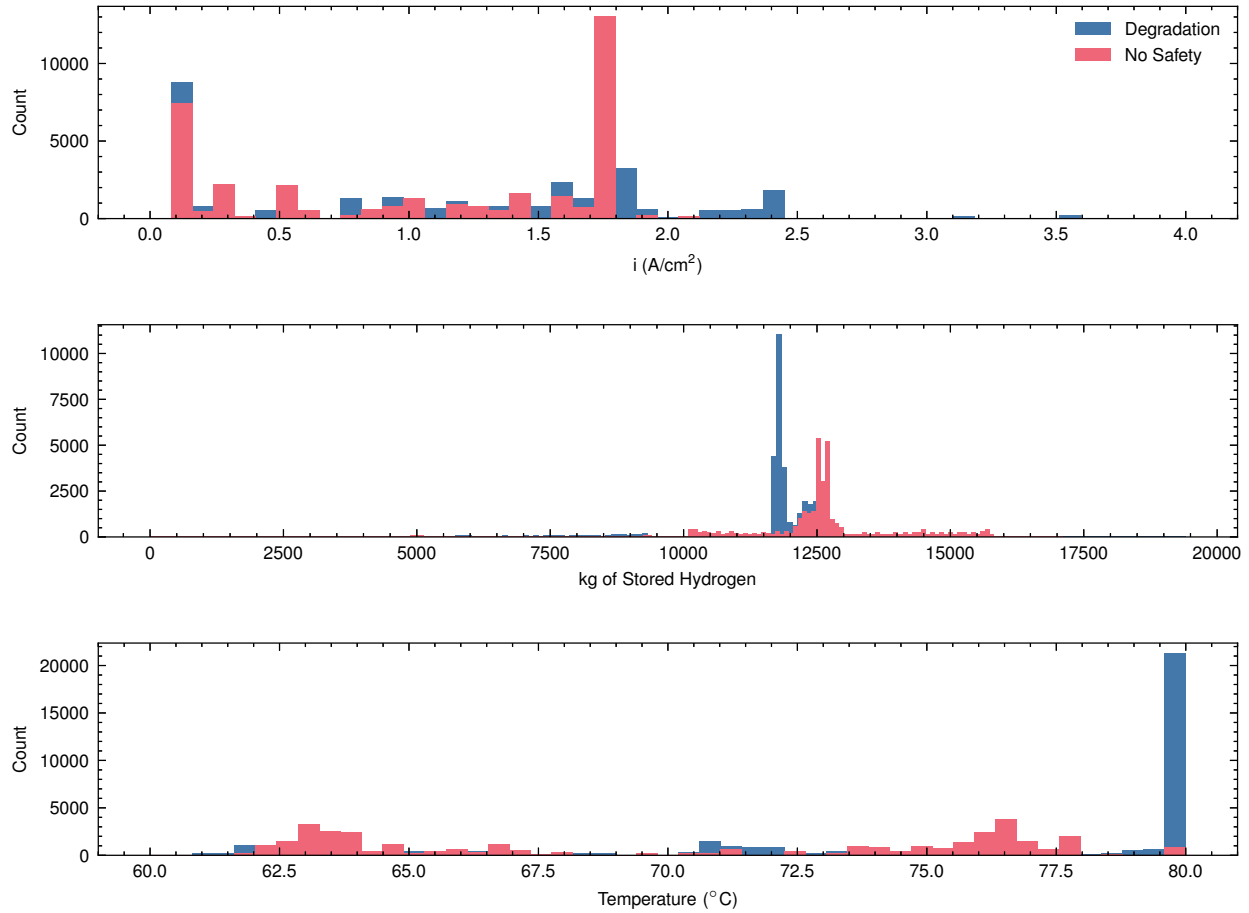


Figure S8: Current density, hydrogen storage, and temperature distributions for the case run without a safety constraint and the base degradation case. With no incentive to keep hydrogen concentration at the anode low, the current density distribution shifts to lower current densities.

5.6.5 Future Scenarios

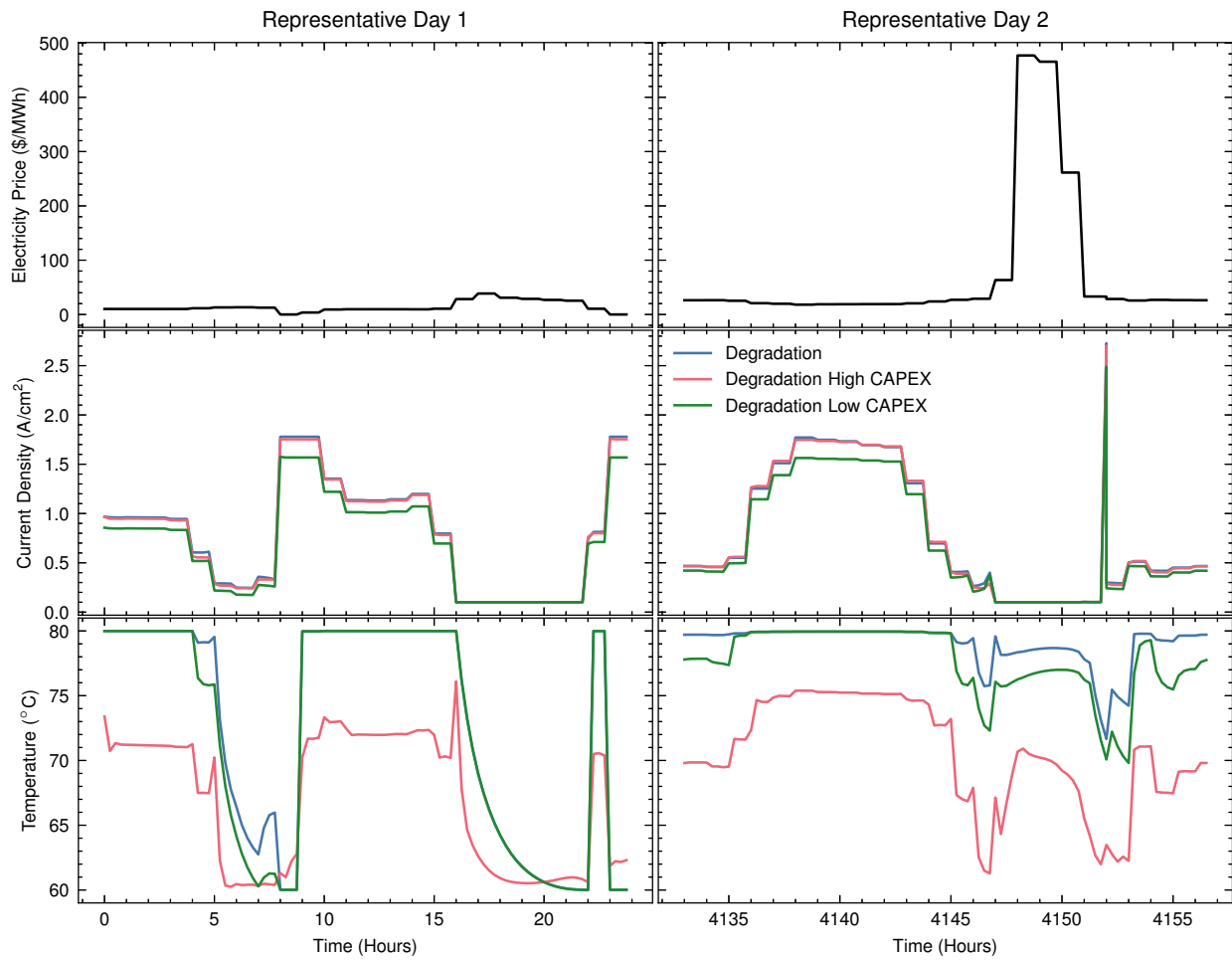


Figure S9: Temperature profile of future CAPEX cases. Generally, the high CAPEX case with more cells operates at lower temperatures due to lower current density and therefore lower overpotential.

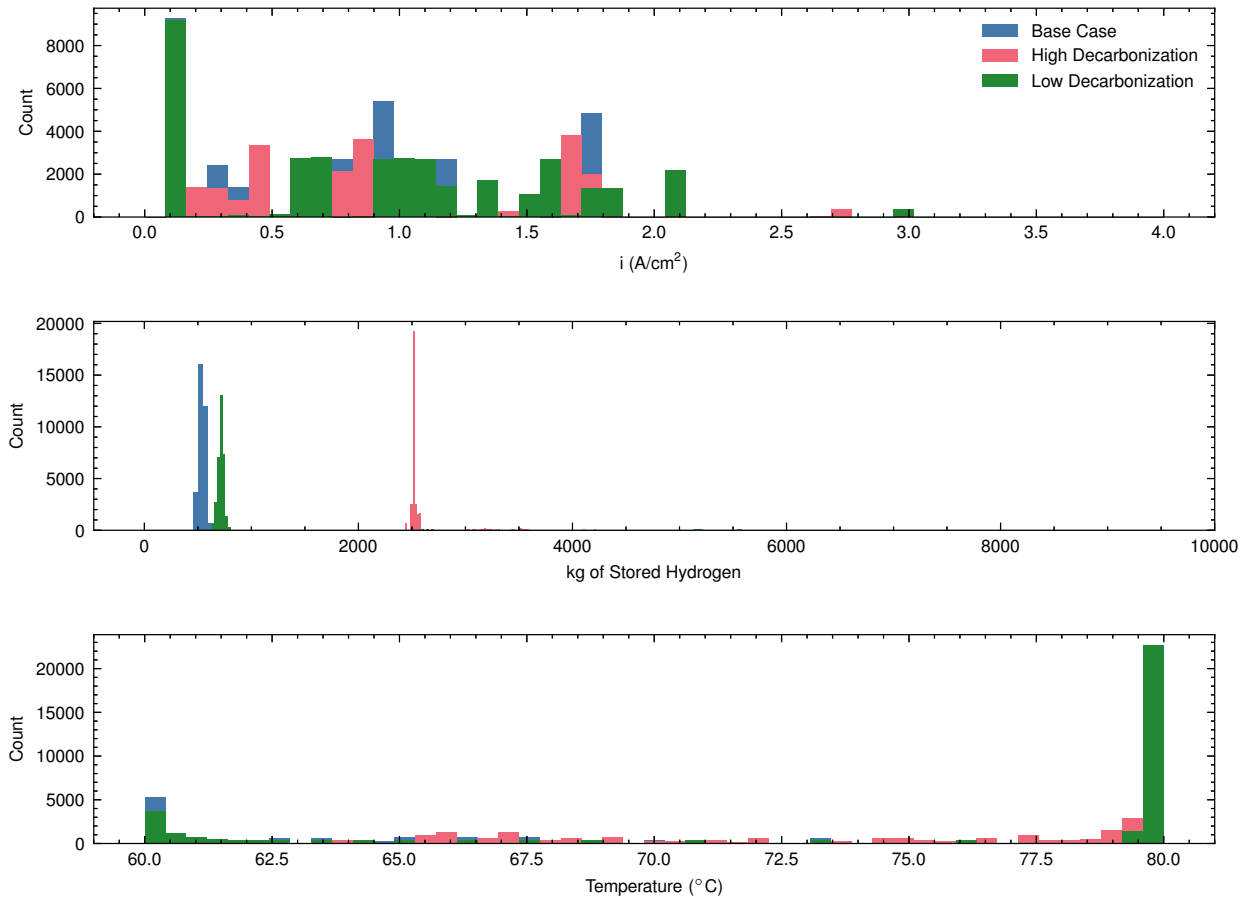


Figure S10: Distribution of current density, hydrogen storage, and temperature for the future cases run with low, mid, and high decarbonized grids. Price scenario corresponding to high grid decarbonization leads to sizing greater storage and operating at lower current densities. Lower grid decarbonization based price scenarios allows for operation at higher current densities because of the lower price of electricity. However, these effects largely do not affect the LCOH (see Table 2).

References

- [1] Brian D James, Daniel A DeSantis, Genevieve Saur. *Final Report: Hydrogen Production Pathways Cost Analysis (2013 – 2016)*. Tech. rep. Strategic Analysis Inc, Sept. 2016.
- [2] Z Abdin, C J Webb, and E Maca Gray. “Modelling and simulation of a proton exchange membrane (PEM) electrolyser cell”. In: *Int. J. Hydrogen Energy* 40.39 (Oct. 2015), pp. 13243–13257.
- [3] Vincenzo Liso, Giorgio Savoia, Samuel Simon Araya, Giovanni Cinti, and Søren Knudsen Kær. “Modelling and Experimental Analysis of a Polymer Electrolyte Membrane Water Electrolysis Cell at Different Operating Temperatures”. en. In: *Energies* 11.12 (Nov. 2018), p. 3273.
- [4] P Medina and M Santarelli. “Analysis of water transport in a high pressure PEM electrolyzer”. In: *Int. J. Hydrogen Energy* 35.11 (June 2010), pp. 5173–5186.
- [5] Donald R Burgess. “Thermochemical Data”. In: *NIST Chemistry WebBook, NIST Standard Reference Database Number 69*. Ed. by P J Linstrom and W G Mallard. Gaithersburg MD, 20899: National Institute of Standards and Technology.
- [6] Manuel Espinosa-López, Christophe Darras, Philippe Poggi, Raynal Glises, Philippe Baucour, André Rakotonrainibe, Serge Besse, and Pierre Serre-Combe. “Modelling and experimental validation of a 46 kW PEM high pressure water electrolyzer”. In: *Renewable Energy* 119 (Apr. 2018), pp. 160–173.
- [7] Maximilian Bernt, Alexandra Hartig-Weiß, Mohammad Fathi Tovini, Hany A El-Sayed, Carina Schramm, Jonas Schröter, Christian Gebauer, and Hubert A Gasteiger. “Current challenges in catalyst development for PEM water electrolyzers”. en. In: *Chem. Ing. Tech.* 92.1-2 (Jan. 2020), pp. 31–39.
- [8] Haluk Görgün. “Dynamic modelling of a proton exchange membrane (PEM) electrolyzer”. In: *Int. J. Hydrogen Energy* 31.1 (Jan. 2006), pp. 29–38.
- [9] *ERCOT Market Prices*. en. <https://www.ercot.com/mktinfo/prices>. Accessed: 2023-11-16.
- [10] Pieter Gagnon, Brady Cowiestoll, and Marty Schwarz. *Cambium 2022 Scenario Descriptions and Documentation*.
- [11] Water Innovations Inc. *Operating Cost for WDI Deionized Water System*. Tech. rep.
- [12] John Harb Thomas Fuller. “Chapter 3 - Electrochemical Kinetics”. In: *Electrochemical Engineering*.
- [13] D S Falcão and A M F R Pinto. “A review on PEM electrolyzer modelling: Guidelines for beginners”. In: *J. Clean. Prod.* 261 (July 2020), p. 121184.
- [14] M Maier, K Smith, J Dodwell, G Hinds, P R Shearing, and D J L Bretta. *Mass Transport in PEM Water Electrolysers: A Review*.
- [15] Christopher Bryce Capuano, Morgan Elizabeth Pertosos, Nemanja Danilovic. “Membrane Electrode Assembly and Method of Making the Same”. 2018/0062192 A1. Mar. 2018.
- [16] Eric Mayousse Nicolas Guillet. “Membrane Electrode Assembly for an Electrolysis Device”. 20140116877 A1. May 2014.
- [17] M Bernt, J Schröter, M Möckl, and H A Gasteiger. “Analysis of Gas Permeation Phenomena in a PEM Water Electrolyzer Operated at High Pressure and High Current Density”. en. In: *J. Electrochem. Soc.* 167.12 (Aug. 2020), p. 124502.